

# 1 **Parameter**Sensitivity Study of Energy Transfer Between 2 Mesoscale Eddies and Wind-Induced Near-Inertial Oscillations

3 Yu Zhang<sup>1</sup>, Jintao Gu<sup>1</sup>, Shengli Chen<sup>1\*</sup>, Jianyu Hu<sup>2</sup>, Jinyu Sheng<sup>3</sup>, Jiuxing Xing<sup>1</sup>

4 <sup>1</sup>Institute for Ocean Engineering, Shenzhen International Graduate School, Tsinghua University, Shenzhen, 518055,  
5 China

6 <sup>2</sup>State Key Laboratory of Marine Environmental Science, College of Ocean and Earth Sciences, Xiamen University,  
7 Xiamen, 361102, China

8 <sup>3</sup>Department of Oceanography, Dalhousie University, Halifax, NS B3H 4R2, Canada

9 *Correspondence to:* Shengli Chen (shenglichen@sz.tsinghua.edu.cn)

10 **Abstract.** Analyses of current observations and numerical simulations at two moorings in the  
11 northern South China Sea reveal the transfer of near-inertial energy between the background  
12 currents associated with mesoscale eddies and near-inertial currents (NICs). A series of numerical  
13 experiments are conducted to determine important parameters affecting the energy transfer  
14 between idealized mesoscale eddies and NICs generated by rotating winds. Speeds of NICs  
15 transferred by both cyclonic and anticyclonic mesoscale eddies increase linearly with the wind  
16 stress and eddy strength. The transferred NICs in anticyclonic eddies have current amplitudes of  
17 about six times larger than in cyclonic eddies. The translation speed of the mesoscale eddy and the  
18 wind rotation frequency also affect the conversion of NICs. The energy transfer rate is elevated  
19 with the increase of the positive Okubo-Weiss parameter. A simple theoretical analysis is  
20 conducted to verify our findings based on numerical results. Analytical solutions confirm the  
21 evident asymmetry of the energy transfer between anticyclonic and cyclonic eddies, and  
22 demonstrate quantitatively the relationship between the wind stress and the near-inertial energy  
23 transferred by mesoscale eddies.

## 24 **1 Introduction**

25 Near-inertial oscillations (NIOs) are very common in the global ocean and they appear as a  
26 prominent peak in the spectrum of ocean currents (Garrett, 2001). NIOs contain almost half the  
27 total kinetic energy of the internal waves and significantly contribute to the vertical shear in the  
28 internal waveband (Ferrari & Wunsch, 2009). When surface winds with high spatiotemporal

设置了格式: 字体: (中文) 宋体, (中文) 简体中文(中国大陆)

29 variations act at the ocean surface, strong NIOs could occur in the ocean surface mixed layer (SML,  
30 Chen et al., 2015a; D'Asaro et al. 1995; Pollard & Millard, 1970). At the base of the SML, near-  
31 inertial internal waves (NIWs) are generated through the horizontal convergence and divergence  
32 of the SML (Gill, 1984). These NIWs are free to radiate to the thermocline and deep waters, and  
33 low-mode NIWs with long wavelengths can propagate at least hundreds of kilometers toward the  
34 equator from their source regions (Alford, 2003; Jochum et al., 2013; Munk & Wunsch, 1998).  
35 NIOs not only affect the energy, momentum, and material transport in the upper ocean, but also  
36 play an important role in maintaining diapycnal mixing and global ocean circulation (Chen et al.,  
37 2016; Greatbatch, 1984; Price et al., 1986; Wunsch & Ferrari, 2004).

38 Due to the turbulent and inhomogeneous nature of the ocean, the central frequency of NIOs  
39 is influenced by the  $\beta$  effect and shows a significant blue or red shift induced by the relative  
40 vorticity of mesoscale eddies (Chen et al., 2015b; Elipot et al., 2010; Kunze, 1985; Mooers, 1975;  
41 Perkins, 1976; Sun et al., 2011). If the magnitude of the gradient in the relative vorticity is larger  
42 than the  $\beta$  effect (Chelton et al. 2011), mesoscale eddies also modulate the energy distribution and  
43 propagation of the near-inertial motions (van Meurs, 1998; Wang et al., 2024). Previous studies of  
44 current observations in the northwestern South China Sea (nSCS) demonstrated that the near-  
45 inertial energy propagates both upwards and downwards under the influence of the anticyclonic  
46 eddies (Chen et al., 2013; Zhai et al., 2007). Using the in situ observations and ray-tracing  
47 techniques, Jaimes and Shay (2010) demonstrated that anticyclonic eddies trap the near-inertial  
48 kinetic energy which rapidly propagates vertically below the thermocline and even to the deep  
49 ocean. Young and Jelloul (1997) suggested that the anticyclonic eddies can improve the vertical  
50 propagation rate of the near-inertial energy by deepening the thermocline. Zhai et al. (2005)  
51 demonstrated that the wind generated near-inertial kinetic energy is also high in the strong  
52 mesoscale motion regions. Based on the numerical study, Lelong et al. (2020) reveled that  
53 anticyclonic eddies facilitate the energy transfer from wind-driven inertial energy to propagating  
54 waves. Fer et al. (2018) found that subinertial waves trapped within the Lofoten Basin eddy can  
55 significantly contribute to the observed turbulence in the eddy.

56 Mesoscale eddies and NIOs are energetic in the SML (Bühler & McIntyre, 2005; Vanneste,  
57 2013; Xie & Vanneste, 2015). Mesoscale eddies not only change the spatial distribution of NIOs,  
58 but also exchange the energy with NIOs through the nonlinear interaction (Muller, 1976; Thomas,  
59 2012). Based on the observational studies of specific NIO events, Noh and Nam (2020) found that

mesoscale eddies can effectively enhance the intensity of NIOs. The energy transfer also occurs between NIOs and low-frequency geostrophic currents through the nonlinear interaction (Liu et al., 2023; Thomas, 2012; Whalen et al., 2020). Jing et al. (2018) demonstrated that the large-scale geostrophic currents of the Gulf Stream affect the distribution of near-inertial energy. Whitt and Thomas (2015) suggested that, in a unidirectional laterally sheared geostrophic flow, a continuous energy transfer occurs between mesoscale eddies and NIOs. In the Kuroshio extension, due to the change of the effective Coriolis frequency caused by the relative vorticity of mesoscale eddies, the energy exchange efficiency between the anticyclonic eddies and NIOs is about twice that between the cyclonic eddies and NIOs (Jing et al., 2017). Based on numerical results in the Icelandic Basin, Barkan et al. (2021) found that a significant energy transfer occurs between NIOs and sub-inertial motions, with the energy transfer rate in winter and summer are about half and a quarter of the local near-inertial wind energy input, respectively. The above and other studies suggested that the energy transfer processes between mesoscale eddies and NIOs should play an important role in the ocean energy cascade (Alford et al., 2016; Ford et al., 2000; McWilliams, 2016; Thomas, 2017). Nevertheless, most of previous studies focused on the energy transfer rate and efficiency. There is a knowledge gap in the amplitude of the near-inertial energy transferred by the mesoscale eddy and the sensitivity of the above-mentioned energy transfer to mesoscale eddies and wind parameters. The main objective of this study is to quantity the energy transfer between the mesoscale eddies and wind-induced NIOs.

This paper is structured as follows. Section 2 provides a brief description of observational data and reanalysis used in this study. Section 3 presents the original and modified slab models. Model results for the energy transfer between mesoscale eddies and the NIOs are given in Sect. 4. A series of sensitivity experiments for determining the important factors affecting the energy transfer is presented in Sect. 5. The results of sensitivity experiments are verified through theoretical analysis in Sect. 6. Summary and discussions are given in Sect. 7.

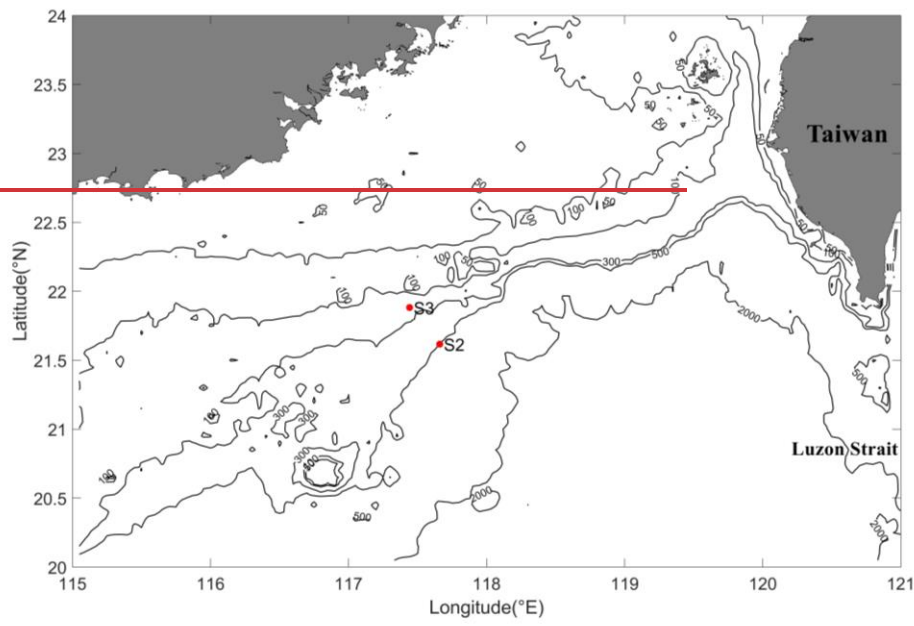
## 2 Observational and Reanalysis Data

Current observations at two subsurface moorings named S2 and S3 respectively in the nSCS (marked in Fig. 1) are analyzed here. The current observations at these two moorings were made using the Acoustic Doppler Current Profilers (ADCPs). Mooring S2 is located at 117°39.619' E and 21°37.001' N, with the water depth of 499 m. Current observations at this location were made

90 at depth bins from 58 m to 442 m from 22 August 2016 to 8 May 2017. At ADCP mooring S2, the  
91 vertical sampling interval is 16 m and the time internal is 60 minutes. ADCP mooring S3 is located  
92 at 117°26.528' E and 21°52.945' N, with the water depth of 266 m. Current observations at this  
93 mooring were made at depth bins from 37 m to 229 m during the same observational period as at  
94 location S2. At mooring S3, the vertical sampling interval is 8 m and the time internal is 30 minutes.

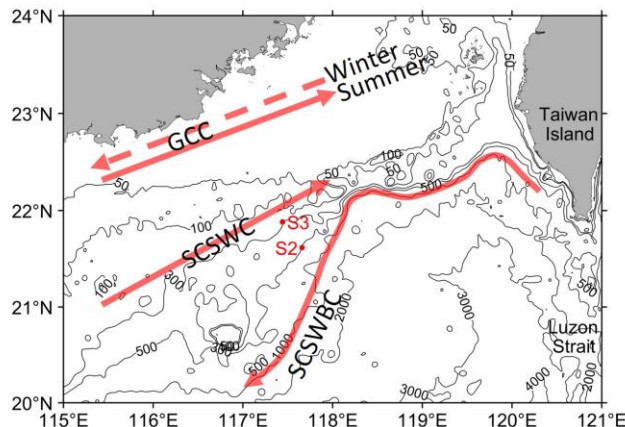
95 Hourly winds at 10 m above the mean sea level in the nSCS were extracted from the European  
96 Centre for Medium-Range Weather Forecasts (ECMWF) ERA5 reanalysis. The ERA5 winds from  
97 July 2016 to June 2017 with an interval of 1 hour and the horizontal resolution of 0.25° are used  
98 to calculate the hourly wind stress to be used as the model forcing. The wind speed data obtained  
99 from ERA5 is widely used in previous researches on near-inertial motions in the Northwestern  
100 Pacific.

101 The surface geostrophic currents used in this study were derived from ECMWF, using the sea  
102 level grid data inferred from the global marine satellite observations provided by the Copernicus  
103 Atmosphere Monitoring Service (C3S). The sea surface height anomaly and geostrophic current  
104 data in the nSCS from July 2016 to June 2017 are used here, which have a horizontal resolution of  
105 0.25° and a time interval of 24 hours.  
106 The mixed layer depth (MLD) for the nSCS was extracted from the 2018 edition of the World  
107 Ocean Atlas (WOA2018) ([www.ncei.noaa.gov/products/world-ocean-atlas](http://www.ncei.noaa.gov/products/world-ocean-atlas)), with a horizontal  
108 resolution of 0.25°. The MLD at each location is defined as the depth at which the vertical change  
109 of the potential density from the ocean surface is 0.125 (sigma units).



110  
111  
112

带格式的: 段落间距段前: 0 磅, 行距: 1.5 倍行距



113

114 **Figure 1.** Major bathymetric feature [and circulation \(from Shu et al., 2018\)](#) of the northern South  
 115 China Sea. Two red dots represent locations of two ADCP moorings named S2 and S3. Black  
 116 contours represent isobaths in meter. [GCC refers to the Guangdong Coastal Current, SCSWC](#)  
 117 [refers to the South China Sea Warm Current and SCSWBC refers to the South China Sea Western](#)  
 118 [Boundary Current. The solid \(dashed\) line in the GCC indicates the current direction in summer](#)  
 119 [\(winter\).](#)

120

121 **3 Method**

122 **3.1 Strain and Vorticity of a Mesoscale Field**

123 The vertical component of the relative vorticity ( $\zeta$ ) has been used to measure the rate of fluid  
 124 rotation within a mesoscale eddy, which is defined as

$$125 \quad \zeta = \frac{\partial V}{\partial x} - \frac{\partial U}{\partial y}, \quad (1)$$

126 where  $U$  and  $V$  are zonal (eastward) and meridional (northward) surface geostrophic currents,  
 127 respectively.

128 [The effective Coriolis frequency \( \$f\_{eff}\$ \) is defined as](#)

$$129 \quad f_{eff} = f + \frac{\zeta}{2} \quad (2)$$

130 [where  \$f\$  is the inertial frequency.](#)

131 The normal and shear components of the rate of strain tensor,  $S_n$  and  $S_s$  are defined as

$$132 \quad S_n = \frac{\partial U}{\partial x} - \frac{\partial V}{\partial y}, \quad (23)$$

$$133 \quad S_s = \frac{\partial V}{\partial x} + \frac{\partial U}{\partial y}. \quad (24)$$

134 The relative importance of total strain and relative vorticity is diagnosed with the Okubo-  
 135 Weiss parameter (Okubo 1970):

$$136 \quad OW = S_n^2 + S_s^2 - \zeta^2. \quad (45)$$

137 In this study, the dependence of the energy transfer between the mesoscale eddy and NICs on  
 138 the relative vorticity is considered.

带格式的: 行距: 单倍行距

设置了格式: 字体颜色: 文字 1

设置了格式: 字体颜色: 文字 1

设置了格式: 字体颜色: 文字 1

设置了格式: 字体颜色: 文字 1

带格式的: 右, 段落间距段后: 0 磅, 行距: 1.5 倍行距, 制表位: 22 字符, 居中 + 44 字符, 右对齐

带格式的: 行距: 单倍行距

139 **3.2 Modified Slab Model**

140 A simple linear model known as the slab model (Pollard & Millard 1970) was used in  
 141 simulating NIOs in the SML. Analysis of observed currents in the nSCS (to be discussed in Sect.  
 142 4) demonstrates that NIOs can also occur in the SML under ~~the~~ nearly steady winds. This suggests  
 143 the importance of the energy transfer between the background currents and near-inertial currents  
 144 (NICs). To investigate this energy transfer, the background geostrophic currents ( $U, V$ ) are added  
 145 to the original slab model as the modified slab model (Jing et al., 2017; Weller, 1982):

$$146 \quad \begin{cases} \frac{\partial u}{\partial t} + u \frac{\partial U}{\partial x} + v \frac{\partial U}{\partial y} = fv - ru + \frac{\tau_x}{\rho_o H_{mix}}, \\ \frac{\partial v}{\partial t} + u \frac{\partial V}{\partial x} + v \frac{\partial V}{\partial y} = -fu - rv + \frac{\tau_y}{\rho_o H_{mix}}, \end{cases} \quad (65)$$

147 where  $(u, v)$  are zonal and meridional currents averaged vertically in the SML, and  $H_{mix}$  is the  
 148 MLD. The damping coefficient  $r$  is set to  $1/8$  days $^{-1}$ , which is used to parameterize the loss of near-  
 149 inertial energy. In Eq. (56),  $f$  is the inertial frequency, and  $\rho_o$  is the seawater density set to be  $1024$   
 150 kg m $^{-3}$ . Wind stress components  $(\tau_x, \tau_y)$  are calculated using ~~10-m height ERA5's 10-m winds~~  
 151 with the drag coefficient suggested by Oey et al. (2006).

152 The above modified slab model uses two important assumptions: the Rossby number of the  
 153 geostrophic currents is assumed to be far less than 1, and the horizontal scale of winds to be much  
 154 larger than that of mesoscale eddies. By ignoring the background geostrophic currents, the above  
 155 modified slab model becomes the original slab model, which was used in many previous studies  
 156 of examining the inertial response in the SML (D'Asaro, 1985; Paduan et al. 1989; Pollard &  
 157 Millard 1970).

158 The modified slab model in Eq. (56) can be solved numerically using an implicit numerical  
 159 scheme in time to obtain NICs in the SML:

$$160 \quad \begin{cases} \frac{u^{n+1}-u^n}{\Delta t} + u^{n+1}U_x^{n+1} + v^{n+1}U_y^{n+1} = fv^{n+1} - ru^{n+1} + \frac{\tau_x^{n+1}}{\rho H_{mix}} \\ \frac{v^{n+1}-v^n}{\Delta t} + u^{n+1}V_x^{n+1} + v^{n+1}V_y^{n+1} = -fu^{n+1} - rv^{n+1} + \frac{\tau_y^{n+1}}{\rho H_{mix}} \end{cases} \quad (67)$$

161 where  $\Delta t$  is the time step, which is set to 3600 s in this study, and subscripts  $x$  and  $y$  in  $U$  and  $V$   
 162 represent partial derivatives. The initial value of the NICs is set to 0. In Eq. (67), variables with  
 163 superscripts  $n$  and  $n + 1$  represent their values at time  $n\Delta t$  and  $(n + 1)\Delta t$ , respectively.

164 After merging some terms, the numerical scheme of the modified slab model can be written

165 as

$$\begin{cases} \frac{u^{n+1}-u^n}{\Delta t} + a_1^{n+1}u^{n+1} + b_1^{n+1}v^{n+1} = c_1^{n+1} \\ \frac{v^{n+1}-v^n}{\Delta t} + a_2^{n+1}u^{n+1} + b_2^{n+1}v^{n+1} = c_2^{n+1}, \end{cases} \quad (78)$$

167 where  $a_1 = U_x + r$ ,  $a_2 = V_x + f$ ,  $b_1 = U_y - f$ ,  $b_2 = V_y + r$ ,  $c_1 = \tau_x/\rho H_{mix}$ ,  $c_2 = \tau_y/\rho H_{mix}$ .

168 Equation (78) can be written in the following tensor form:

$$\begin{bmatrix} a_1^{n+1} + \frac{1}{\Delta t} & b_1^{n+1} \\ a_2^{n+1} & b_2^{n+1} + \frac{1}{\Delta t} \end{bmatrix} \begin{bmatrix} u^{n+1} \\ v^{n+1} \end{bmatrix} = \begin{bmatrix} \frac{u^n}{\Delta t} + c_1^{n+1} \\ \frac{v^n}{\Delta t} + c_2^{n+1} \end{bmatrix}. \quad (89)$$

170 The numerical update equations for currents are given as

$$u^{n+1} = \frac{1 + \Delta t b_2^{n+1}}{(1 + \Delta t a_1^{n+1})(1 + \Delta t b_2^{n+1}) - \Delta t b_1^{n+1} a_2^{n+1}} \left[ \frac{u^n}{\Delta t} + c_1^{n+1} - \frac{\Delta t b_1^{n+1}}{1 + \Delta t b_2^{n+1}} \left( \frac{v^n}{\Delta t} + c_2^{n+1} \right) \right], \quad (910)$$

$$v^{n+1} = \frac{1 + \Delta t a_1^{n+1}}{(1 + \Delta t a_1^{n+1})(1 + \Delta t b_2^{n+1}) - \Delta t b_1^{n+1} a_2^{n+1}} \left[ \frac{u^n}{\Delta t} + c_1^{n+1} - \frac{\Delta t a_2^{n+1}}{1 + \Delta t a_1^{n+1}} \left( \frac{v^n}{\Delta t} + c_2^{n+1} \right) \right]. \quad (110)$$

### 173 3.3 Analysis of NICs

174 The observed zonal and meridional currents at 58.3 m below the sea surface at location S2  
 175 and at 37.7 m at location S3 (marked in Fig. 1) in the nSCS are analyzed to estimate the near-  
 176 inertial kinetic energy in the SML. The observed NICs are obtained by using a band-pass filter  
 177 [through Fourier transform](#) with a frequency band of 0.85f-1.15f.

178 The surface geostrophic currents described in Sect. 2 are specified in the modified slab model,  
 179 based on the assumption that the geostrophic currents are vertically uniform in the SML during  
 180 the study period. The simulated currents by the original and modified slab models are band-passed  
 181 [through Fourier transform](#) with the frequency band of 0.85f-1.15f and are further smoothed using  
 182 a running window of two inertial periods to obtain the simulated [amplitude of NICs](#).

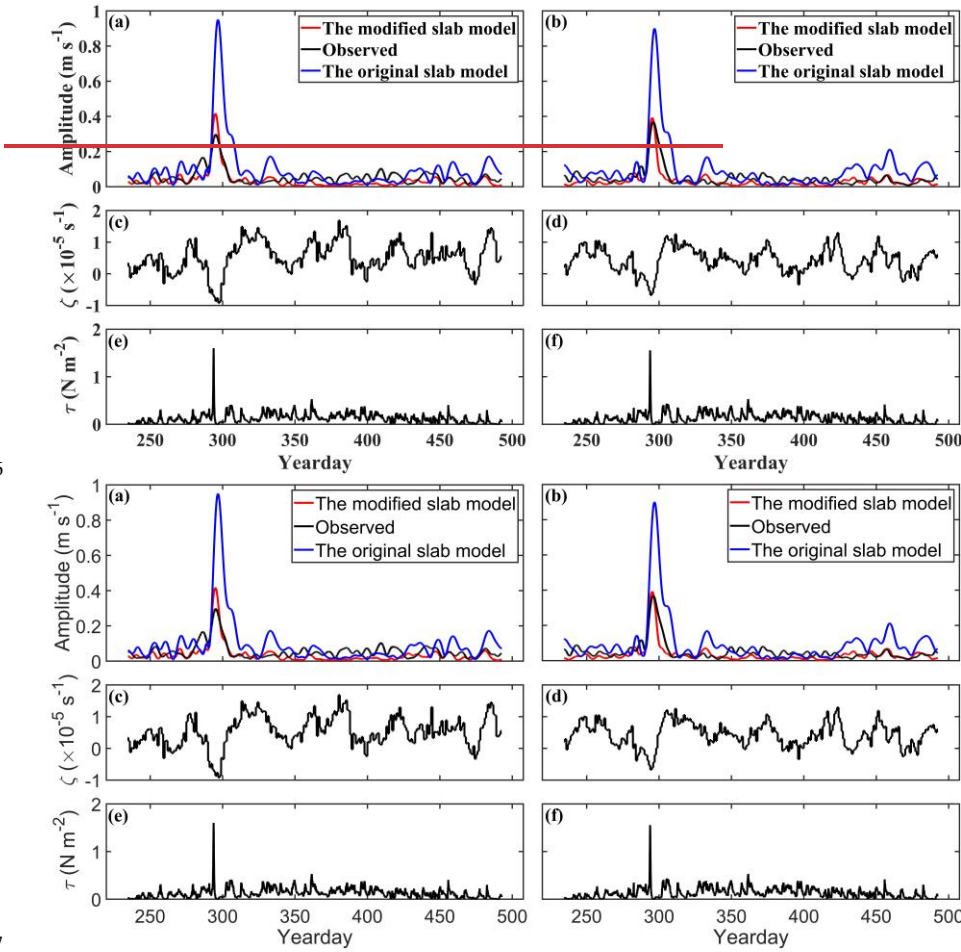
183 To quantitatively assess performances of the original and modified slab models, the  
 184 correlation analysis and root mean square error (RMSE) analysis between the original slab model,  
 185 the modified slab model and observations respectively are made.

186 **4 Results**

187 **4.1 Observed NICs**

188 Time series of observed NICs at the top depth bins (58.3 m at S2 and 37.7 m at S3) of two  
189 subsurface ADCP moorings (known as  $\vec{u}_{S2}^{top}$  and  $\vec{u}_{S3}^{top}$ ) are shown in black lines in Fig. 2 during  
190 the observational period from day 234 (22 August 2016) to day 492 (7 May 2017) with respect to  
191 1 January 2016. Intense NICs were generated and lasted for about 11 days from day 293 to day  
192 304 under the largest wind forcing ( $\sim 1.6 \text{ N m}^{-2}$ ) on day 293 (Fig. 2e and 2f). The largest speed of  
193 NICs was  $\sim 0.30 \text{ m s}^{-1}$  on day 295 at the top depth bin at mooring S2 (Fig. 2a) and  $\sim 0.37 \text{ m s}^{-1}$  on  
194 day 296 at the top depth bin at mooring S3 (Fig. 2b). Some NICs were also excited on other days  
195 when the winds were relatively weak and nearly steady.

196



197

198 **Figure 2.** Speeds ( $\text{m s}^{-1}$ ) of observed (black line) and simulated NICs at the top depth bins of  
199 ADCP observations at moorings (a) S2 and (b) S3. Red and blue lines denote model results  
200 produced by the modified slab and original slab models respectively. Time series of relative  
201 vorticity of the surface geostrophic currents at moorings (c) S2 and (d) S3, and time series of wind  
202 stress at moorings (e) S2 and (f) S3. [The yearday is defined as the number of days elapsed since  
203 00:00:00 \(GMT\) on 1 January 2016. Yearday is the day relative to 00:00:00 \(GMT\) on 1 January  
204 2016.](#)

205

206 Observed NICs at other depth bins of these two ADCP moorings reveal that the intense NICs  
207 occurred on days 293-304 at depths between 60 m and 200 m at mooring S2 (not shown) and these

208 NICs were originated from the SML. At mooring S3, similar intense NICs occurred at depths  
209 between 40 m and 180 m on days 280-305 (not shown), and these NIC were also originated from  
210 the SML. On days 306-318, in comparison, moderate NICs occurred in the lower layer between  
211 150 m and 310 m at these two moorings.

212 It should be noted that the current observations ( $\vec{u}_{S2}^{top}$  and  $\vec{u}_{S3}^{top}$ ) at the top bins of the two  
213 ADCP moorings are in the lower part of the SML or below the SML during the observational  
214 period. Based on WOA2018, the climatological monthly mean MLD at the two ADCP moorings  
215 is the thinnest and ~20 m in August ([days 234-243](#)) and increases to the maximum value of ~90 m  
216 in January ([days 366-396](#)). The MLD decreases from ~56 m in February ([days 397-424](#)) to ~37 m  
217 in May ([days 486-492](#)) and is about 25 m in June and July. This suggests that the observed NICs  
218 at the top depth bin (58.3 m) of S2 were made in the lower part of the SML in December and  
219 January (days 335-396), but below the SML on the other days of the observational period (Fig.  
220 2a). By comparison, the observed NICs at the top depth bin (37.7 m) of S3 were made in the middle  
221 of the SML in December and January (days 335-396), and in the lower part of the SML in October  
222 and November (days 274-334) and February-May (days 397-492).

223 The relative vorticity estimated from the surface geostrophic currents was negative at the two  
224 moorings on days 290-300 (Fig. 2c and 2d), with the maximum negative values of about  $-0.92 \times 10^{-5} \text{ s}^{-1}$  (-0.17f)  
225 at mooring S2 and about  $-0.68 \times 10^{-5} \text{ s}^{-1}$  (-0.13f) at mooring S3. The negative values  
226 of the relative vorticity during this period resulted from the westward propagation of an  
227 anticyclonic eddy. As shown in Fig. 3a and 3f, moorings S2 and S3 were located over the area  
228 between a relatively strong anticyclonic eddy and a weak cyclonic eddy on day 295. The  
229 anticyclonic eddy moved westward and passed mooring S2 before day 316 (Fig. 3b and 3g). On  
230 day 316, the relative vorticity was low and positive of about  $1.23 \times 10^{-5} \text{ s}^{-1}$  (0.23f) at mooring S2  
231 and  $0.83 \times 10^{-5} \text{ s}^{-1}$  (0.15f) at mooring S3 respectively.

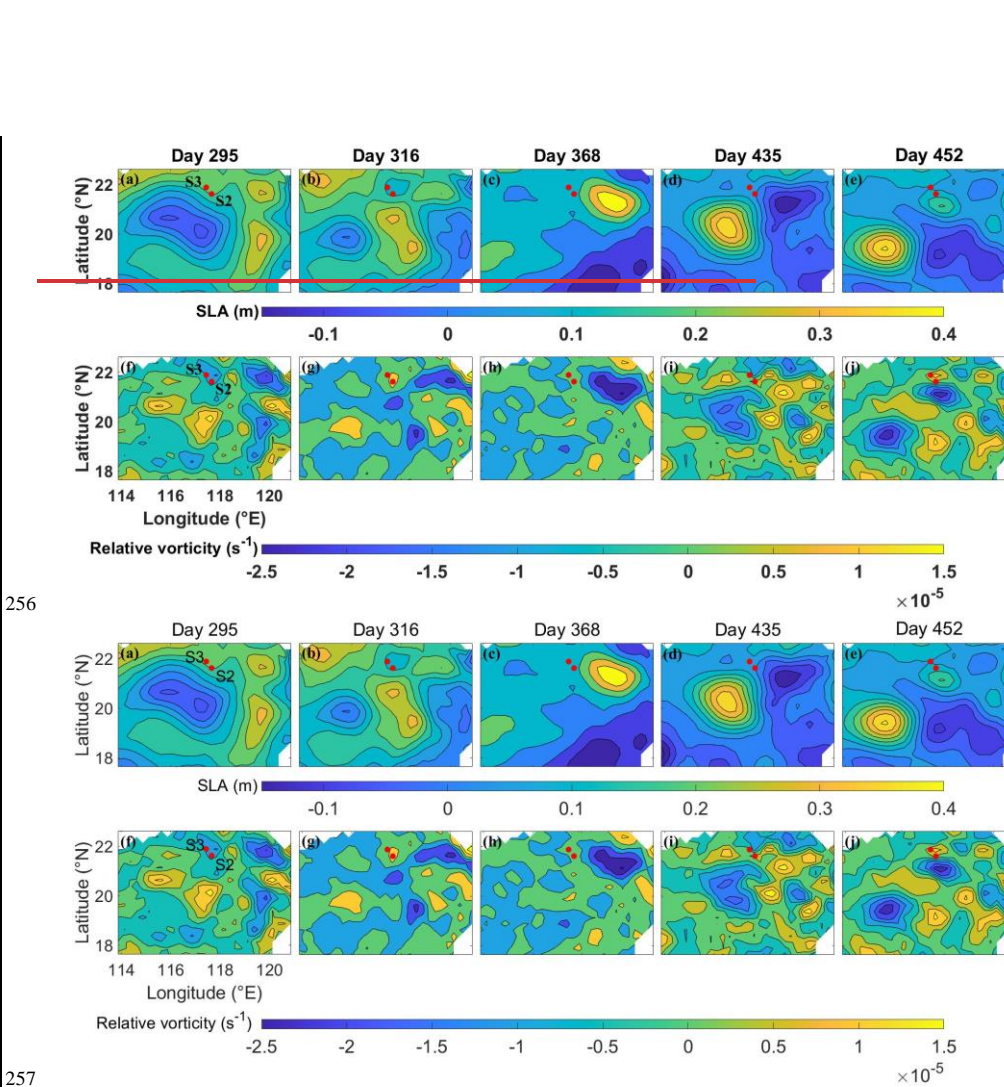
232 On days 350-450, an anticyclonic eddy moved southwestward and passed through these two  
233 moorings S2 and S3 (Fig. 3c, 3d, 3h, and 3i). There was a weak cyclonic eddy close to the two  
234 moorings on day 435 (Fig. 3d and 3i). The relative vorticity was relatively strong and positive  
235 during this period, with the maximum positive values of about  $1.68 \times 10^{-5} \text{ s}^{-1}$  (0.31f) on day 380 at  
236 mooring S2 and  $1.29 \times 10^{-5} \text{ s}^{-1}$  (0.24f) on day 423 at mooring S3 respectively.

237 Between days 451-492, there is a weak anticyclonic eddy close to the moorings S2 and S3 and the  
238 two moorings are located at the edge of the anticyclonic eddy on day 452 (Fig. 3e and 3j).

设置了格式: 字体颜色: 自动设置

239  
240 The relative vorticity estimated from the surface geostrophic currents was negative at the two  
241 moorings on days 290–300 (Fig. 2c and 2d), with the maximum negative values of about  $0.92 \times 10^{-5} \text{ s}^{-1}$   
242 at mooring S2 and about  $0.68 \times 10^{-5} \text{ s}^{-1}$  at mooring S3. The negative values of the relative  
243 vorticity during this period resulted from the westward propagation of an anticyclonic eddy. As  
244 shown in Fig. 3a and 3f, on day 295, moorings S2 and S3 were located over the area between a  
245 relatively strong cyclonic eddy to the southwest and two separate weak cyclonic eddies to the east  
246 and south. The anticyclonic eddy moved westward and passed mooring S2 before day 316 (Fig.  
247 3b and 3g). On day 316, the relative vorticity was low and positive of about  $1.23 \times 10^{-5} \text{ s}^{-1}$  at  
248 mooring S2 and  $0.83 \times 10^{-5} \text{ s}^{-1}$  at mooring S3 respectively. On days 350–450, an anticyclonic eddy  
249 moved westward and passed through these two moorings S2 and S3, and there was a weak cyclonic  
250 eddy close to the two moorings on day 435 (Fig. 3e, 3d, 3h, and 3i). The relative vorticity was  
251 relatively strong and positive during this period, with the maximum positive values of about  
252  $1.68 \times 10^{-5} \text{ s}^{-1}$  on day 380 at mooring S2 and  $1.29 \times 10^{-5} \text{ s}^{-1}$  on day 423 at mooring S3 respectively.  
253 Between days 451–492, there is a weak anticyclonic eddy close to the moorings S2 and S3 and the  
254 two moorings are located at the edge of the anticyclonic eddy on day 452 (Fig. 3e and 3j).

255



258 **Figure 3.** Spatial distributions of sea surface level anomaly (SLA) on day 295 (a), day 316 (b),  
259 day 368 (c), day 435 (d) and day 452 (e). Spatial distributions of the relative vorticity on day 295  
260 (f), day 316 (g), day 368 (h), day 435 (i) and day 452 (j). Two red dots mark locations of two  
261 ADCP moorings S2 and S3.

262 **4.2 Simulated NICs**

263 Numerical simulations are made using the original and modified slab models to examine  
264 whether the energy exchange occurs between the mesoscale eddy and NICs in the SML at  
265 moorings S2 and S3. Both the original and modified slab models assume that the NICs in the SML

266 is vertically uniform and use the damping coefficient  $r$  set to a relatively small value of  $1/8$  day $^{-1}$ .  
267 Both the models are forced by time series of wind stress shown in Fig. 2e and 2f.

268 The simulated NICs produced by the original slab model at the top bins of two ADCP  
269 moorings are shown by the blue lines in Fig. 2a and 2b. The simulated NICs by the original slab  
270 model are large and about  $0.95$  m s $^{-1}$  ( $0.90$  m s $^{-1}$ ) at mooring S2 (S3) on day 296 and relatively  
271 weak on days 350-430. In comparison with the observed NICs, the original slab model has large  
272 deficiency of overpredicting significantly the observed large NICs on days 285-300 at the two  
273 stations and also overpredicting moderately the observed NICs on other days of the observational  
274 period. It should be noted that the results of both the original and modified slab models using three  
275 different damping coefficients ( $r = 1/5$  day $^{-1}$ ,  $1/6$  day $^{-1}$  and  $1/7$  day $^{-1}$ ) and annual mean MLD at  
276 two stations ( $\sim 45$  m) are highly similar with the model results using  $r = 1/8$  day $^{-1}$  and monthly  
277 mean MLD shown in Fig. 2a and 2b.

278 In comparison with the original slab model results, the modified slab model generates much  
279 smaller NICs than the original slab model on days 280-305 (red lines in Fig. 2a and 2b), with the  
280 maximum value of about  $0.42$  m s $^{-1}$  at mooring S2 and about  $0.39$  m s $^{-1}$  at mooring S3 on day 295.  
281 In comparison with the observed NICs at the two moorings, the modified slab model performs  
282 significantly better than the original slab model on days 250-325 and days 451-492, indicating the  
283 importance of the energy exchange between the background mesoscale eddies and NICs. On days  
284 350-450, the relative vorticity of the background currents is positive, which results in the simulated  
285 NICs produced by the modified slab model to be slightly weaker than the observed NICs at these  
286 two moorings. As mentioned in Sect. 4.1, the top depth bins of the ADCP observations at the two  
287 moorings were in the lower part of the SML or below the SML during the observational period,  
288 which explains partially the differences between observed and simulated NICs by the modified  
289 slab model shown in Fig. 2a and 2b. Differences between the observed and simulated NICs can  
290 also partially be explained by the assumption of vertically uniform geostrophic currents in the  
291 SML and exclusion of baroclinic dynamics.

292 The above analysis based on results shown in Fig. 2 suggests that, overall, the simulated NICs  
293 produced by the modified slab model agree with the observed NICs significantly better than the  
294 original slab model at two moorings S2 and S3. This indicates the occurrence of the near-inertial  
295 energy transfer induced by the interaction between mesoscale eddies and NICs in the SML during  
296 the observational period.

297 To quantify the model performance, we use the correlation coefficient (R) and the root mean  
298 square error (RMSE) based on the time series of observed and simulated NICs shown in Fig. 2a  
299 and 2b. The modified slab model has a higher correlation coefficient (R = ~0.81) and smaller root  
300 mean square error (RMSE = ~0.04 m s<sup>-1</sup>) than the original slab model (R = ~0.70 and RMSE =  
301 ~0.12 m s<sup>-1</sup>) at mooring S2. At mooring S3, the R value between the observed NICs and results of  
302 the modified slab model is ~0.84, and RMSE is ~0.03 m s<sup>-1</sup>. For the original slab model at location  
303 S3, the R value is ~0.85, and RMSE is ~0.10 m s<sup>-1</sup>. These statistical indices suggest that the  
304 modified slab model performs better than the original slab model, especially in reproducing the  
305 amplitude of the observed NICs. This also suggests the energy transfer between mesoscale eddies  
306 and NICs may be a non-negligible process in the energy cascade across different scales in the  
307 global ocean.

308

309 **Table 1.** Correlation coefficients (R) and RMSEs between the simulation results of the modified  
310 and original slab models and observations for the observational period, respectively.

Mooring	Correlation coefficient (R)		RMSE (m s <sup>-1</sup> )	
	Original slab model	Modified slab model	Original slab model	Modified slab model
S2	0.70	0.81	0.12	0.04
S3	0.85	0.84	0.10	0.03

311 **5 Sensitivity Study**

312 A series of numerical experiments (in total 22496) are conducted using the original and  
313 modified slab models to examine sensitivity of model results to the wind speed, the wind rotation  
314 frequency, the translational speed of the mesoscale eddy, and the strength of the mesoscale eddy.  
315 Both the cyclonic and anticyclonic eddies with an idealized eddy structure are used for simplicity.  
316 Results of the original and modified slab models are both band-pass (0.60f-1.40f) filtered to get  
317 broad NICs signals and then smoothed using a running window [of two inertial periods](#) to obtain  
318 the near-inertial velocity in the SML.

319 **5.1 Idealized Mesoscale Eddy Structure**

320 Based on the composite analysis of satellite altimetry and Argo float data, Zhang et al. (2013)  
321 suggested a universal structure of mesoscale eddies in the global ocean. Their universal structure  
322 of mesoscale eddies is used in our experiments.

323 The normalized structure  $\tilde{P}(\tilde{r}, z)$  of the pressure anomaly in the universal mesoscale eddy  
 324 used in this study is decomposed into a radial function  $R(\tilde{r})$  and a vertical function  $H(z)$ :

$$325 \quad \tilde{P}(\tilde{r}, z) = R(\tilde{r}) H(z), \quad (1\textcolor{red}{24})$$

$$326 \quad R(\tilde{r}) = \left(1 - \frac{\tilde{r}^2}{2}\right) e^{-\frac{\tilde{r}^2}{2}}, \quad (1\textcolor{red}{32})$$

$$327 \quad H(z_s) = H_0 \sin(kz_s + \theta_0) + H_{ave}, \quad (\textcolor{red}{43}\textcolor{red}{14})$$

$$328 \quad \tilde{r} = \frac{r}{R_0}, \quad (\textcolor{red}{44}\textcolor{red}{15})$$

$$329 \quad z_s = \int_0^z \left(\frac{N}{f}\right) dz, \quad (\textcolor{red}{45}\textcolor{red}{16})$$

330 where  $r$  is the radial distance to the eddy center,  $R_0$  is the radius of the mesoscale eddy,  $N$  is the  
 331 buoyancy frequency,  $H_0$ ,  $k$ ,  $\theta_0$  and  $H_{ave}$  are undetermined coefficients, e.g. in this study,  $H_0 =$   
 332  $2/3$ ,  $H_{ave} = 2/3$ ,  $N = 10^{-3}$  (1/s),  $k = \pi/18000$ ,  $f = 5 \times 10^{-5}$  (rad/s) and  $\theta_0 = \pi/6$ .  
 333 The vertical structure function  $H(z)$  defined above is similar with the structural diagram in Zhang  
 334 et al. (2013).

335 The structure function for the idealized mesoscale eddy in the Cartesian coordinate system  
 336 can be written as

$$337 \quad \tilde{P}(x, y, z) = \left(1 - \frac{x^2+y^2}{2R_0^2}\right) \cdot e^{-\frac{x^2+y^2}{2R_0^2}} \cdot \left[\frac{2}{3} \cdot \sin\left(\frac{\pi}{900} \cdot z + \frac{\pi}{6}\right) + \frac{2}{3}\right], \quad (1\textcolor{red}{76})$$

338 with the origin of the coordinate to be the eddy center at the sea surface.

339 Using the pressure anomaly suggested by Wei et al. (2017), the equation for the pressure field  
 340 based on the different strength of mesoscale eddies can be given as

$$341 \quad P(x, y, z) = P_0 \cdot \tilde{P}(x, y, z) + \bar{P}(z), \quad (1\textcolor{red}{87})$$

$$342 \quad P_0 = g \cdot \rho_0 \cdot SLA_c, \quad (1\textcolor{red}{98})$$

343 where  $P_0$  is the strength of mesoscale eddies,  $\rho_0$  is the reference density of seawater taken as  
 344  $1024 \text{ kg/m}^3$ ,  $g$  is the gravitational acceleration set to be  $9.8 \text{ m/s}^2$ ,  $SLA_c$  is the sea surface level  
 345 anomaly (SLA) of the eddy center where the anticyclone eddies are specified as negative values  
 346 and the cyclonic eddies are positive values, and the average pressure field is denoted by  $\bar{P}$ . As only  
 347 mesoscale eddy signals are added to the ocean in this study,  $\bar{P}$  is a function of the vertical direction  
 348 that is homogeneous in the horizontal direction.

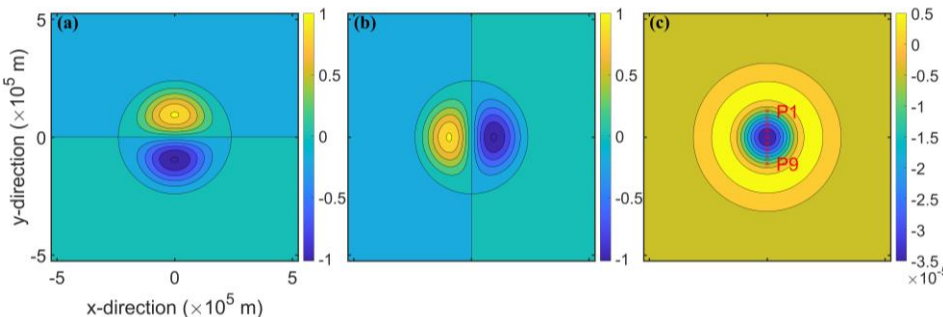
349 Using the geostrophic balance, the zonal and meridional components of the geostrophic  
 350 velocity at the ocean surface are given as

351 
$$u = -\frac{1}{\rho_0 f} \frac{\partial P}{\partial y} = -\frac{P_0}{\rho_0 f} \left[ \frac{y^3 + yx^2 - 4yR_0^2}{2R_0^4} \right] e^{-\frac{x^2+y^2}{2R_0^2}}, \quad (2.19)$$

352 
$$v = \frac{1}{\rho_0 f} \frac{\partial P}{\partial x} = \frac{P_0}{\rho_0 f} \left[ \frac{x^3 + xy^2 - 4xR_0^2}{2R_0^4} \right] e^{-\frac{x^2+y^2}{2R_0^2}}. \quad (2.10)$$

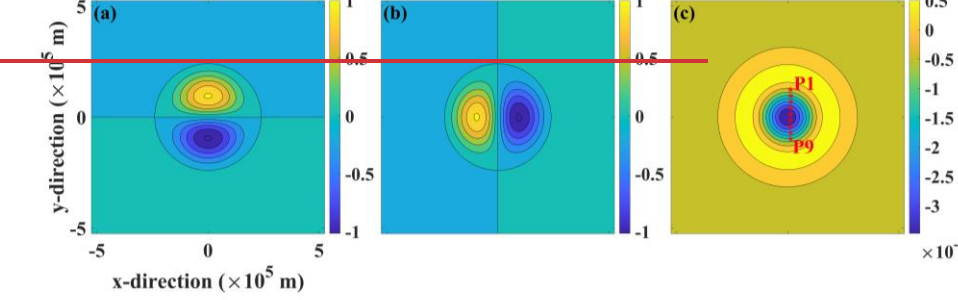
353 In this study, the cyclonic and anticyclonic eddies are set to have the same strength with the  
 354 opposite relative vorticity. Numerical experiments are conducted with the idealized mesoscale  
 355 eddy moving westward. Figure 4 shows currents and relative vorticity at the sea surface for an  
 356 idealized anticyclonic eddy with the radius of 120 km,  $R_0$  to be 120 kilometers, and  $P_0$  of  
 357 6400 kg/m · s<sup>2</sup> (i.e.,  $SLA_c$  is equal to 0.64 m), and the core Rossby number of about -0.7. Based  
 358 on Eq. (4.19), the mesoscale eddy strength  $P_0$  is a positive proportional function of the  $SLA_c$  under  
 359 the constant seawater density and gravitational acceleration. The strength of the mesoscale eddy  
 360 can be characterized by the absolute values of the  $SLA_c$  ( $|SLA_c|$ ).

361 To examine model results inside the eddy, nine fixed locations in space named P1-P9 along  
 362 the y-axis (marked in Fig. 4c) are selected. The distance from the eddy center to P1 (P9) is  $0.92R_0$ ,  
 363 to P2 (P8) is  $0.69R_0$ , to P3 (P7) is  $0.46R_0$ , and to P4 (P6) is  $0.23R_0$ . After the wind-driven currents  
 364 reach a steady state, the mesoscale eddy propagates westward to reach the area of interest (P1-P9).  
 365 The zonal and meridional components of currents for an anticyclonic eddy increase from the center  
 366 to the edge of the eddy, and then gradually decrease outside the anticyclonic eddy (Fig. 4a and 4b).  
 367 The relative vorticity is largest at the eddy center and then reduces gradually from the center to the  
 368 edge of the eddy (Fig. 4c). The idealized eddy exhibits has a velocity reversal from the eddy center  
 369 outward, which forms a circular positive (negative) vorticity around the periphery of the idealized  
 370 anticyclonic (cyclonic) eddy in the Northern Hemisphere (Zhang et.al 2013).  
 371



带格式的: 缩进: 首行缩进: 0 字符

带格式的: 居中, 缩进: 首行缩进: 0 字符, 行距: 单倍行距



373

374 **Figure 4.** Distributions of (a) zonal ( $u$ ) and (b) meridional ( $v$ ) components ( $\text{m s}^{-1}$ ) of currents and  
 375 (c) relative vorticity ( $\text{s}^{-1}$ ) for an idealized anticyclonic eddy with a radius of 120 km. Model results  
 376 at nine fixed locations (P1-P9) denoted by red asterisks along the  $y$ -axis in (c) are examined.

377

378 Jing et al. (2017) proposed a method to calculate the efficiency of energy transfer from  
 379 background mesoscale eddies to wind-induced NICs. In this study, we use the differences in the  
 380 average speeds of NICs between the modified and original model ( $\text{NICs}_U_{AE}$  and  $\text{NICs}_U_{CE}$ ) as  
 381 the proxies for the near-inertial energy generated in the mesoscale eddies by the interaction  
 382 between mesoscale eddies and NICs:

383 
$$\text{NICs}_U_{AE} = \text{NICs}_U_{AE}^{\text{Modified}} - \text{NICs}_U_{AE}^{\text{Original}}, \quad (2.24)$$

384 
$$\text{NICs}_U_{CE} = \text{NICs}_U_{CE}^{\text{Modified}} - \text{NICs}_U_{CE}^{\text{Original}}, \quad (2.25)$$

385 where  $\text{NICs}_U_{AE}^{\text{Modified}}$  ( $\text{NICs}_U_{AE}^{\text{Original}}$ ) and  $\text{NICs}_U_{CE}^{\text{Modified}}$  ( $\text{NICs}_U_{CE}^{\text{Original}}$ ) are the averaged  
 386 speeds of NICs based on results produced by the modified (original) slab model in the anticyclonic  
 387 eddies and cyclonic eddies over the same time period, respectively. It should be noted that the  
 388 simulated NICs by the original slab model represent the near-inertial energy generated directly by  
 389 the wind forcing. Therefore, after removing the generation of wind-induced NICs, the differences  
 390  $\text{NICs}_U_{AE}$  and  $\text{NICs}_U_{CE}$  represent the amplitudes of NICs transferred by interactions between  
 391 mesoscale eddies and NICs in the anticyclonic eddies and the cyclonic eddies respectively.

392 To quantify differences in the NICs transferred by background currents between the  
 393 anticyclonic and cyclonic eddies, we introduce a simple parameter  $\alpha$ , defined as

394 
$$\alpha = \frac{\text{NICs}_U_{AE}}{\text{NICs}_U_{CE}}. \quad (2.26)$$

395 If  $\alpha$  is larger than 1, it means that the anticyclonic eddy can transfer more NICs than the cyclonic  
396 eddy with the same strength.

397 **5.2 Effect of Wind Speeds**

398 The wind speed affects the energy input from the wind to the SML, and therefore influences  
399 interaction between mesoscale eddies and NICs. To facilitate theoretical analysis and generate a  
400 reasonable magnitude of the NICs speeds, we conduct the numerical experiments using  
401 cyclonically rotating winds and anticyclonically rotating and in the Northern Hemisphere with the  
402 constant wind speed (A). The wind stress  $\tau$  used in our sensitivity study takes a form as follows

$$403 \quad \tau_x(t) + i \tau_y(t) = A e^{iBt}, \quad (254)$$

404 where  $\tau_x(t)$  and  $\tau_y(t)$  are time-dependent zonal and meridional components of wind stress, and  
405  $B$  is the wind rotation frequency. Positive wind rotation frequencies represent cyclonically  
406 rotating winds and negative wind rotation frequencies indicate anticyclonically rotating winds.

407 Five numerical experiments (ExpA1-5) are conducted with the background idealized  
408 mesoscale eddy moving westward with a translational speed of  $8 \text{ cm s}^{-1}$ . The  $|SLA_c|$  of both  
409 anticyclonic and cyclonic eddies are set to  $0.64 \text{ m}$  in these five experiments. The speeds (A) of  
410 time-varying winds in these five experiments are set to  $5 \text{ m s}^{-1}$ ,  $10 \text{ m s}^{-1}$ ,  $13 \text{ m s}^{-1}$ ,  $15 \text{ m s}^{-1}$ , and  $20$   
411  $\text{m s}^{-1}$  respectively, corresponding to wind stress amplitudes of  $0.038 \text{ N m}^{-2}$ ,  $0.150 \text{ N m}^{-2}$ ,  $0.282 \text{ N}$   
412  $\text{m}^{-2}$ ,  $0.412 \text{ N m}^{-2}$ , and  $0.876 \text{ N m}^{-2}$  respectively. The wind forcing rotates cyclonically at the inertial  
413 frequency  $f$ . The conclusions drawn from the average and the sum of nine locations (P1-P9) are  
414 consistent. The magnitude of the sum is larger than that of the average, which makes the  
415 presentation of the results clearer and more intuitive.

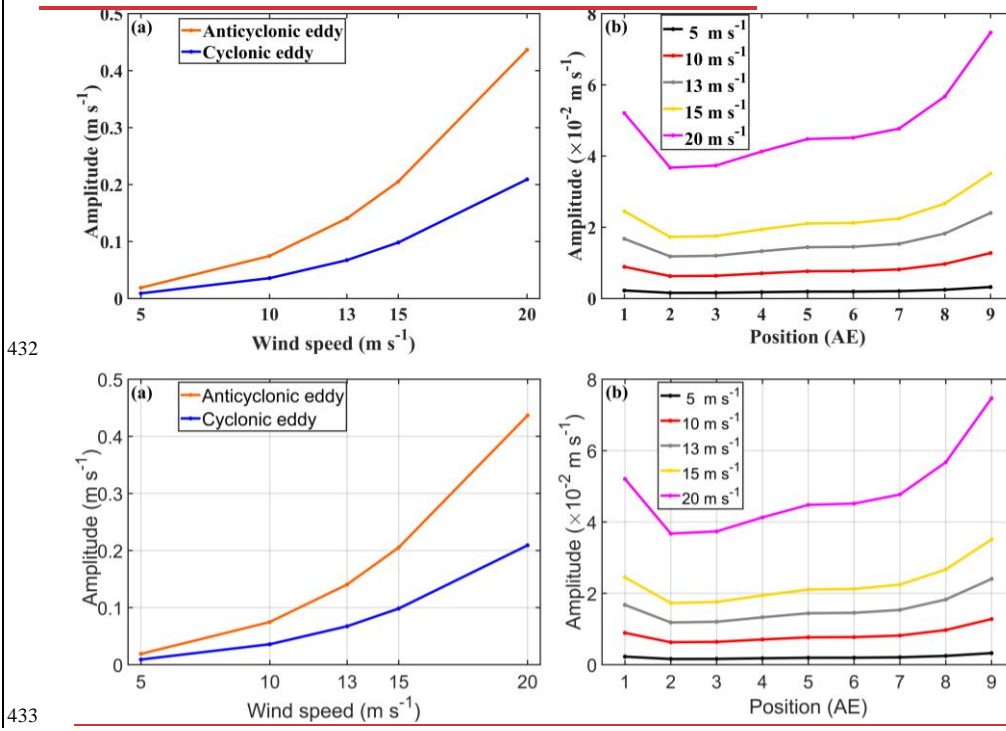
416 For a cyclonic eddy with  $|SLA_c| = 0.64 \text{ m}$ , the sum of averaged speeds of NICs converted  
417 from this cyclonic eddy at the above-mentioned nine locations ( $\sum \text{NICs}_U_{CE}$ ) are about  $0.009 \text{ m s}^{-1}$   
418 and  $0.209 \text{ m s}^{-1}$  for cyclonic wind speeds of  $5 \text{ m s}^{-1}$  (i.e.  $0.038 \text{ N m}^{-2}$ ) and  $20 \text{ m s}^{-1}$  (i.e.  $0.876 \text{ N}$   
419  $\text{m}^{-2}$ ) respectively (Fig. 5a). This suggests that, within the cyclonic eddy, the  $\sum \text{NICs}_U_{CE}$  increases  
420 23 times if the cyclonic wind stress increases 23 times, which is consistent with the conclusion  
421 based on the analytical solution in Sect. 6.

422 In an anticyclonic eddy with the same strength of  $|SLA_c| = 0.64 \text{ m}$ , the sum of averaged  
423 speeds of NICs transferred from this anticyclonic eddy at the nine locations ( $\sum \text{NICs}_U_{AE}$ ) also

424 increases with the wind speeds. The  $\sum \text{NICs}_\text{U}_{AE}$  values are about  $0.019 \text{ m s}^{-1}$  and  $0.437 \text{ m s}^{-1}$  for  
 425 the cyclonic wind speeds of  $5 \text{ m s}^{-1}$  (corresponding to  $0.038 \text{ N m}^{-2}$ ) and  $20 \text{ m s}^{-1}$  (corresponding to  
 426  $0.876 \text{ N m}^{-2}$ ) respectively (Fig. 5a). This indicates that the averaged speeds of NICs generated in  
 427 anticyclonic eddies by the interaction between background anticyclonic eddies and NICs also  
 428 increase linearly with the cyclonic wind stress, 23 times if the cyclonic wind stress increases 23  
 429 times. But the NICs are stronger in the anticyclonic eddy than in the cyclonic eddy under the same  
 430 wind conditions.

431

带格式的: 缩进: 首行缩进: 2 字符



432  
 433  
 434 **Figure 5.** (a) Sum of averaged speeds of transferred NICs at 9 fixed locations P1-P9 as a function  
 435 of the wind speeds in the anticyclonic eddy (orange line) and cyclonic eddy (blue line), respectively.  
 436 (b) Averaged speeds of transferred NICs as a function of the wind speeds in the anticyclonic eddy.  
 437 The black, red, gray, yellow and purple line indicate respectively the wind speed of  $5 \text{ m s}^{-1}$  (ExpA1),  
 438  $10 \text{ m s}^{-1}$  (ExpA2),  $13 \text{ m s}^{-1}$  (ExpA3),  $15 \text{ m s}^{-1}$  (ExpA4) and  $20 \text{ m s}^{-1}$  (ExpA5). Numbers on the  
 439 horizontal axis in (b) denote nine fixed locations P1 to P9. The wind rotates cyclonically at the

440 inertial frequency. Mesoscale eddies move westward at the translational speed of  $8 \text{ cm s}^{-1}$  and  
441  $|SLA_c| = 0.64 \text{ m}$ .

442

443 It should be noted that, however, the transferred near-inertial energy varies with the actual  
444 locations within the mesoscale eddy. We take the example of anticyclonic eddies to illustrate this  
445 issue. In anticyclonic eddies, the difference between nine locations P1-P9 is large (Fig. 5b). The  
446 amplitude shows a distribution characterized by small values at the eddy center and relatively large  
447 values at the eddy edge, and this distribution characteristic is more obvious with the increase of  
448 the wind speed. The amplitudes of transferred NICs decrease outward from the eddy edge and are  
449 small in the rim of the mesoscale eddy.

450 -The Okubo-Weiss parameter increases radially outward from the center of the mesoscale  
451 eddy. When the wind speed is relatively small, the difference of the energy generation induced by  
452 the Okubo-Weiss parameter is not significant (Fig. 5b). With the increase of the wind energy input,  
453 the larger absolute value of the positive Okubo-Weiss parameter gradually has the decisive  
454 function in the energy transfer. Therefore, it makes the anticyclonic eddy exhibit superior energy  
455 conversion characteristics at the eddy edge, which is consistent with the conclusion based on the  
456 energy transfer rate (Fig. 10).

457 The  $\alpha$  values (Eq. (2324)) are about 2.08 based on the sum of averaged speeds of NICs at the  
458 nine locations in the five different wind speeds. This indicates that the anticyclonic eddy is more  
459 efficient than the cyclonic eddy in transferring the kinetic energy to NICs (Fig. 5a). The difference  
460 in the near-inertial energy transfer efficiency between anticyclonic and cyclonic eddies is not  
461 affected very much by magnitudes of wind speeds.

### 462 5.3 Effect of Wind Rotation Frequencies

463 The rotation frequency of the winds can affect the generation of the NICs and thus the energy  
464 transfer between the mesoscale eddy and NICs, therefore ~~six-28~~ numerical experiments using  
465 different wind rotation frequencies ( ~~$\pm 1.5f$ ,  $\pm 1.25f$ ,  $\pm 1.4f$ ,  $\pm 0.91.15f$ ,  $\pm 1.10.75f$ ,  $\pm$~~   
466  ~~$10.05f$ ,  $\pm 0.25f$ ,  $\pm 0.925f$ ,  $\pm 0.90.5f$ ,  $\pm 0.80.75f$ ,  $\pm 0.8f$ ,  $\pm 0.75f$ ,  $\pm 0.51.25f$  and  $\pm$~~   
467  ~~$0.254.5f$~~ , where  $f$  is the inertial frequency), denoted as ExpB1-~~1328~~, are conducted. Positive wind  
468 rotation frequencies correspond to cyclonically rotating winds, and negative wind rotation  
469 frequencies are for anticyclonically rotating winds. In these ~~thirteen-28~~ experiments, the mesoscale

470 eddy moves westward at the speed of  $8 \text{ cm s}^{-1}$  and  $|SLA_c| = 0.64 \text{ m}$ . The winds rotate at different  
471 frequencies and the wind speed is set to  $13 \text{ m s}^{-1}$ .

472 Figure 6 shows the sum of averaged speeds of the transferred NICs at the nine locations as  
473 function of the wind rotation frequency for the cyclonic and anticyclonic eddies. Under  
474 cyclonically rotating and anticyclonically rotating wind conditions, there is bidirectional energy  
475 transfer between mesoscale eddies and NICs. The closer the absolute value of the wind rotation  
476 frequency to  $f$ , the stronger the energy transfer between mesoscale eddies and NICs. When the  
477 wind rotation frequency is negative, the wind rotation direction is the same as that of the local  
478 NICs. Wind rotation frequencies close to the inertial frequency of  $-f$  can lead to the resonance and  
479 induce large NICs. Therefore, the strong NICs provide a significant energy source for reverse  
480 energy conversion, allowing the near-inertial kinetic energy to be reabsorbed into the background  
481 mesoscale eddies and contribute to the reconstruction of the geostrophic balance.

482 For cyclonic eddies, the sum of averaged speeds of NICs ( $\sum \text{NICs}_U_{CE}$ ) is sensitive to the  
483 wind rotation frequency. The  $\sum \text{NICs}_U_{CE}$  values are less than zero when the winds rotate  
484 cyclonically at the frequencies of  $0.25f$ ,  $0.75f$  and  $1.25f$  (Fig. 6b) and the winds rotate  
485 anticyclonically at frequencies ranging from  $-1.15f$  to  $-0.75f$  (Fig. 6a), indicating that direction  
486 of the energy transfer is from the NICs to the cyclonic eddies. The amplitudes of the energy  
487 transferred from NICs to cyclonic eddies under anticyclonically rotating wind conditions are larger  
488 than those transferred under cyclonically rotating wind conditions. The addition of mesoscale  
489 eddies has a damping effect for NICs, leading to the negative energy transfer that aligns with the  
490 observed results (Fig. 2). When the direction of the energy transfer is positive, the  $\sum \text{NICs}_U_{CE}$  has  
491 a maximum value of about  $0.635 \text{ m s}^{-1}$  when the winds rotate anticyclonically at the frequency of  
492  $-1.25f$ .

493 For anticyclonic eddies, the sum of averaged speeds of NICs ( $\sum \text{NICs}_U_{AE}$ ) also varies with  
494 the wind rotating frequency. When the winds rotate anticyclonically at frequencies ranging from  $-$   
495  $1.5f$  to  $-0.9f$ , the direction of the energy transfer is from NICs to anticyclonic eddies (Fig. 6a).  
496 The negative energy transfer is strongest at the resonance frequency of  $-f$ . The  $\sum \text{NICs}_U_{AE}$  values  
497 are all positive under cyclonically rotating winds, which represent the energy transfer from the  
498 anticyclonic eddies to NICs (Fig. 6b). The  $\sum \text{NICs}_U_{AE}$  values for the anticyclonic eddies increases  
499 from the value of  $\sim 0.002 \text{ m s}^{-1}$  at the wind rotating frequency of  $0.25f$  to the maximum value of  
500  $\sim 0.213 \text{ m s}^{-1}$  at the wind rotating frequency of  $0.90f$ . The  $\sum \text{NICs}_U_{AE}$  values are larger than the

501  $\sum \text{NICs}_\text{CE}$  values under the same positive wind rotation frequency. The closer the rotational  
502 frequency of the cyclonic winds is to the inertial frequency, the greater the difference in near-  
503 inertial energy conversion induced by anticyclonic eddies and cyclonic eddies.

带格式的: 缩进: 首行缩进: 0 字符

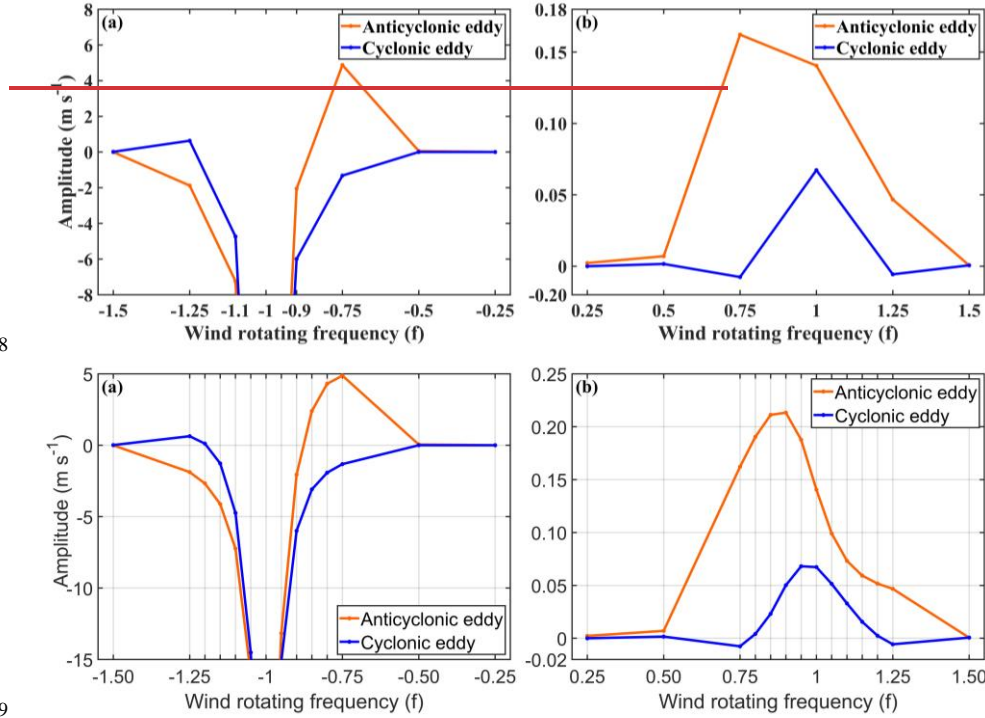
504  
505  
506 For cyclonic eddies, the sum of averaged speeds of NICs ( $\sum \text{NICs}_\text{CE}$ ) is sensitive to the wind  
507 rotation frequency. The  $\sum \text{NICs}_\text{CE}$  values are less than zero when the winds rotate cyclonically  
508 at the frequencies of  $0.25f$ ,  $0.75f$  and  $1.25f$  (Fig. 6b) and the winds rotate anticyclonically at the  
509 frequencies of  $1.1f$ ,  $0.9f$  and  $0.75f$  (Fig. 6a), indicating that direction of the energy transfer is  
510 from the NICs to the cyclonic eddies. The amplitudes of the energy transferred from NICs to  
511 cyclonic eddies under anticyclonically rotating wind conditions are larger than those transferred  
512 under cyclonically rotating wind conditions. The addition of mesoscale eddies has a damping  
513 effect for NICs, leading to the negative energy transfer that aligns with the observed results (Fig.  
514 2). When the direction of the energy transfer is positive, the  $\sum \text{NICs}_\text{CE}$  has a maximum value of  
515 about  $0.635 \text{ m s}^{-1}$  when the winds rotate anticyclonically at the frequency of  $1.25f$ .

516 For anticyclonic eddies, the sum of averaged speeds of NICs ( $\sum \text{NICs}_\text{AE}$ ) also varies with the  
517 wind rotating frequency. When the winds rotate anticyclonically at frequencies of  $1.5f$ ,  $1.25f$ ,  
518  $1.1f$  and  $0.9f$ , the direction of the energy transfer is from NICs to anticyclonic eddies (Fig. 6a).  
519 The negative energy transfer is strongest at the frequency of  $1.1f$ . The  $\sum \text{NICs}_\text{AE}$  values are all  
520 positive under cyclonically rotating winds, which represent the energy transfer from the  
521 anticyclonic eddies to NICs (Fig. 6b). The  $\sum \text{NICs}_\text{AE}$  values for the anticyclonic eddies increases  
522 from the value of  $-0.002 \text{ m s}^{-1}$  at the wind rotating frequency of  $0.25f$  to the maximum value of  
523  $-0.162 \text{ m s}^{-1}$  at the wind rotating frequency of  $0.75f$ . The  $\sum \text{NICs}_\text{AE}$  values are larger than the  
524  $\sum$  values under the same positive wind rotation frequency. The closer the rotational frequency  
525 of the cyclonic winds is to the inertial frequency, the greater the difference in near inertial energy  
526 conversion induced by anticyclonic eddies and cyclonic eddies.

527

528

529



530 **Figure 6.** Sum of averaged speeds of transferred NICs at 9 fixed locations P1-P9 as a function of  
 531 rotation frequencies of (a) anticyclonically rotating winds and (b) cyclonically rotating winds. The  
 532 orange and blue line indicate respectively the anticyclonic eddy and cyclonic eddy. The wind  
 533 rotation frequencies are normalized by the inertial frequency  $f$ .

534 **5.4 Effect of Eddy Translational Speeds**

535 The translational speed of a background mesoscale eddy defines the forcing duration of winds  
 536 and thus the energy input to NICs in the ocean SML. Based on the observations of mesoscale  
 537 eddies in the nSCS, nine numerical experiments (ExpC1-9) using different translational speeds of  
 538 mesoscale eddies ( $4 \text{ cm s}^{-1}$ ,  $5 \text{ cm s}^{-1}$ ,  $6 \text{ cm s}^{-1}$ ,  $7 \text{ cm s}^{-1}$ ,  $8 \text{ cm s}^{-1}$ ,  $9 \text{ cm s}^{-1}$ ,  $10 \text{ cm s}^{-1}$ ,  $11 \text{ cm s}^{-1}$ , and  
 539  $12 \text{ cm s}^{-1}$ ) are conducted. In these nine experiments, the speed of cyclonically rotating winds at the  
 540 inertial frequency is set to  $13 \text{ m s}^{-1}$ . The mesoscale eddy moves westward and  $|SLA_c| = 0.64 \text{ m}$ .

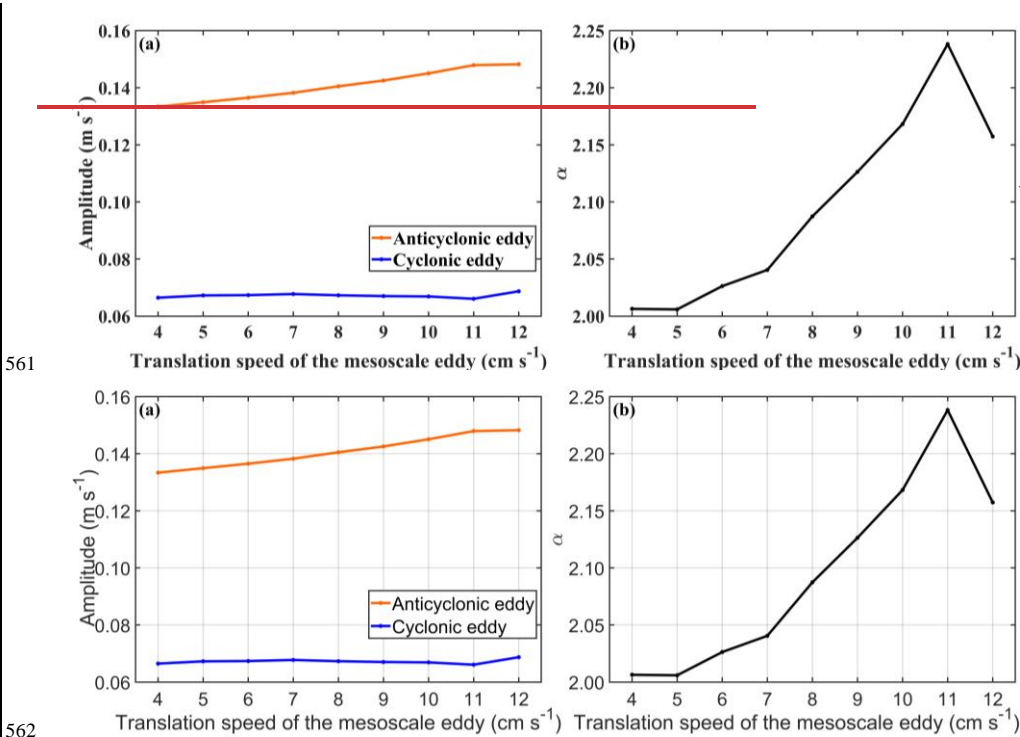
541 For the anticyclonic eddy with  $|SLA_c| = 0.64 \text{ m}$ , the sum of average speeds of the converted  
 542 NICs at the nine locations ( $\sum \text{NICs}_U_{AE}$ ) increases from about  $0.133 \text{ m s}^{-1}$  to  $0.148 \text{ m s}^{-1}$  as the

543 translational speeds increase from  $4 \text{ cm s}^{-1}$  to ~~12~~11  $\text{cm s}^{-1}$  (Fig. 7a). After the translational speed  
544 reaches 11 cm/s, the value of  $\sum \text{NICs}_A \text{U}_{AE}$  remains almost the same as that at a translational speed  
545 of 11 cm/s. The increase of the translational speed enhances the total kinetic energy of mesoscale  
546 eddies, which can provide a larger energy source and be more beneficial for the conversion of  
547 NICs. The translational speed of the mesoscale eddy is smaller than the maximum rotation speed  
548 of the mesoscale eddy. It should be noted that the change in the eddy kinetic energy caused by the  
549 different translational speeds is relatively small in comparison with the total eddy energy  
550 determined by the mesoscale eddy strength. Therefore, the change in the amplitude of the  
551 transferred NICs is relatively small.

552 For a cyclonic eddy with  $|SLA_c| = 0.64 \text{ m}$ , the sum of average speeds of the transferred NICs  
553 at the nine locations ( $\sum \text{NICs}_A \text{U}_{CE}$ ) range from  $0.066 \text{ m s}^{-1}$  to  $0.069 \text{ m s}^{-1}$  and are not sensitive to  
554 the translational speeds (Fig. 7a). Same as in the anticyclonic eddy case, more total kinetic energy  
555 is available for generating NICs within the cyclonic eddy with the same structure but with the  
556 faster translational speeds. Different from the anticyclonic eddy case, however, the anticyclonic  
557 eddy is not conducive to the energy transfer to NICs naturally. Therefore, the slightly larger energy  
558 source caused by the increase of the translational speeds has little influence on the total amount of  
559 kinetic energy transferred from the cyclonic eddy to NICs.

560

带格式的: 缩进: 首行缩进: 2 字符



带格式的: 左

563     Figure 7. (a) Sum of averaged speeds of transferred NICs at 9 fixed locations P1-P9 as a function  
564     of the eddy translational speed in the anticyclonic eddy (orange line) and cyclonic eddy (blue line),  
565     respectively. (b) The  $\alpha$  value as a function of the eddy translational speed. The speed of the  
566     cyclonic wind is  $13 \text{ m s}^{-1}$ , and the wind rotates at the inertial frequency. Mesoscale eddies move  
567     westward and  $|SLA_c| = 0.64 \text{ m}$ .

568  
569     The  $\alpha$  value has a maximum value of  $\sim 2.24$  occurring at the eddy translational speeds of  $11$   
570      $\text{cm s}^{-1}$  (Fig. 7b). This means that the anticyclonic eddy transfers much more near-inertial energy  
571     than the cyclonic eddy does, particularly at the translational speed of  $11 \text{ cm s}^{-1}$ . After exceeding the  
572     translational speed of  $11 \text{ cm s}^{-1}$ , the  $\alpha$  values decrease with the increase of the eddy translational  
573     speeds. The  $\alpha$  value is  $\sim 2.16$  at the translational speed of  $12 \text{ cm s}^{-1}$ . The average speeds of the  
574     NICs at the mesoscale eddy edge are generally larger than that of at the mesoscale eddy center.

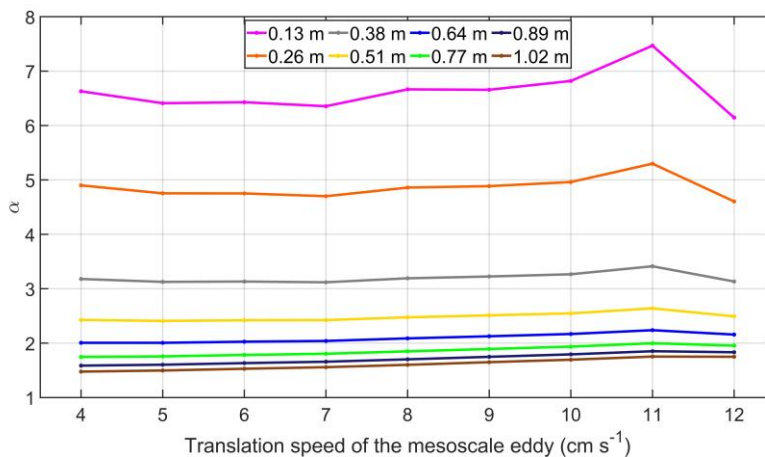
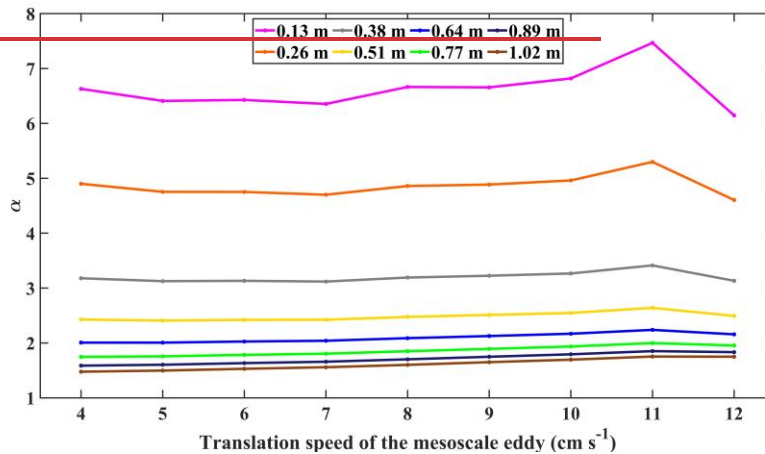
575     A natural question arises whether the variations of  $\alpha$  values within the mesoscale eddy are  
576     affected by the strength of anticyclonic eddies. To address this issue, we consider the sum of

577 averaged speeds of NICs at nine locations for mesoscale eddies and the  $\alpha$  values with different  
 578 strengths and translational speeds (Fig. 8). We consider the case with the cyclonically rotating  
 579 wind speed of  $13 \text{ m s}^{-1}$  at the inertial frequency. For mesoscale eddies with larger  $|SLA_c|$  values,  
 580 the  $\alpha$  values are relatively less sensitive to the translational speed. For mesoscale eddies with  
 581 different  $|SLA_c|$  values, the  $\alpha$  values all have the maximum values with the translational speeds of  
 582  $11 \text{ cm s}^{-1}$ . The  $\alpha$  value decreases with the elevated translational speed when the eddy translational  
 583 speed is larger than  $11 \text{ cm s}^{-1}$ .

584

带格式的: 缩进: 首行缩进: 2 字符

带格式的: 左



587     **Figure 8.** The  $\alpha$  values at 9 fixed locations P1-P9 as a function of the strengths and translational  
588     speeds of the mesoscale eddies. The speed of the cyclonically rotating winds at the inertial  
589     frequency is  $13 \text{ m s}^{-1}$ . Mesoscale eddies move westward. Different colors of lines represent  
590     different mesoscale eddy strengths.

591

592     **5.5 Effect of Mesoscale Eddy Strengths**

593     In addition to the effect of the eddy translational speed, other characteristics of mesoscale  
594     eddies such as the radius and strength of mesoscale eddies can also affect the energy exchange.  
595     Sixteen numerical experiments (denoted as ExpD1-16) are conducted in this section using various  
596     strengths of mesoscale eddies. In these sixteen experiments, the speed of cyclonically rotating  
597     winds at the inertial frequency is set to  $13 \text{ m s}^{-1}$ , the translational speed of mesoscale eddies is set  
598     to  $8 \text{ cm s}^{-1}$ , and the eddy translational direction to be westward. The  $|SLA_c|$  values are set to 0.13  
599     m, 0.26 m, 0.38 m, 0.51 m, 0.64 m, 0.77 m, 0.89 m, and 1.02 m for cyclonic and anticyclonic  
600     eddies, respectively.

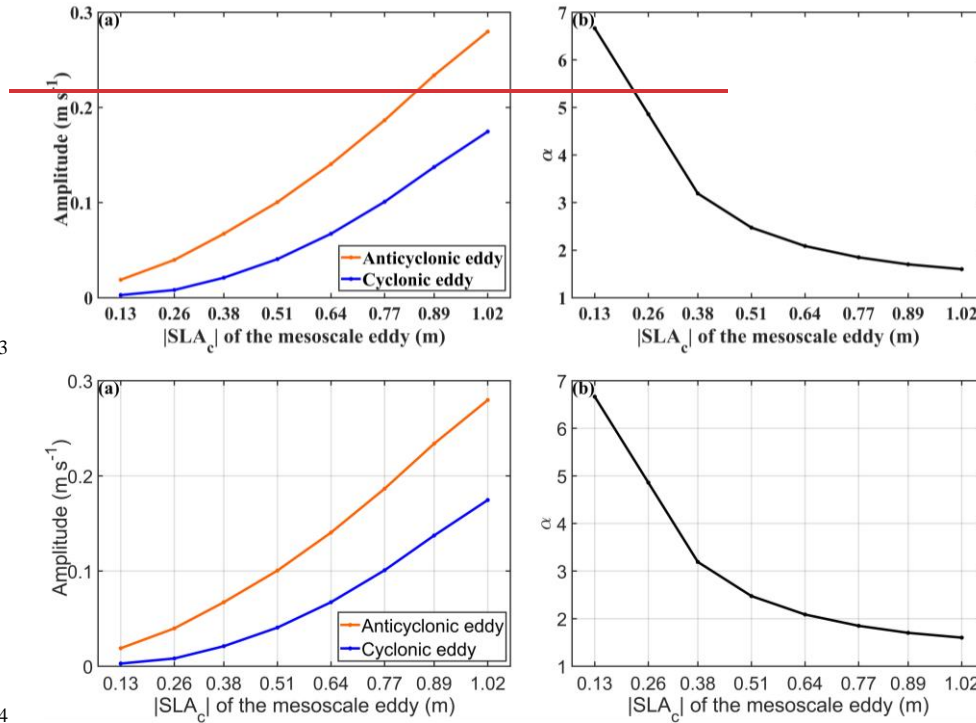
601     Figure 9a shows that the sum of averaged speeds of the transferred NICs at nine locations as  
602     a function of the mesoscale eddy strengths for the cyclonic ( $\sum \text{NICs}_U_{CE}$ ) and anticyclonic eddies  
603     ( $\sum \text{NICs}_U_{AE}$ ). Both values of  $\sum \text{NICs}_U_{AE}$  and  $\sum \text{NICs}_U_{CE}$  are larger for higher eddy strengths,  
604     particularly for the anticyclonic eddies. For the  $|SLA_c|$  values equal to 0.13 m, values of  
605      $\sum \text{NICs}_U_{AE}$  and  $\sum \text{NICs}_U_{CE}$  are about  $0.019 \text{ m s}^{-1}$  and about  $0.003 \text{ m s}^{-1}$ . The averaged speeds of  
606     the converted NICs increase with the  $|SLA_c|$  value, particularly for the anticyclonic eddies. For  
607      $|SLA_c| = 1.02 \text{ m}$ , the averaged speeds of the transferred NICs are  $\sim 0.280 \text{ m s}^{-1}$  and  $\sim 0.175 \text{ m s}^{-1}$   
608     for the anticyclonic and cyclonic eddies respectively, which are  $\sim 14.74$  times and  $\sim 58.33$  times  
609     larger than the counterparts at  $|SLA_c| = 0.13 \text{ m}$ . As the geostrophic strain field is relatively stronger  
610     at the eddy edge, the average speeds of the converted NICs at the mesoscale eddy edge are larger  
611     than that at the mesoscale eddy center.

612

带格式的: 缩进: 首行缩进: 2 字符

613

614



615 **Figure 9.** (a) Sum of averaged speeds of transferred NICs at 9 fixed locations P1-P9 as a function  
 616 of the strengths ( $|SLA_c|$ ) of the mesoscale eddy) of the anticyclonic eddy (orange line) and cyclonic  
 617 eddy (blue line). (b) The  $\alpha$  value as a function of the eddy strengths ( $|SLA_c|$ ) of the mesoscale eddy.  
 618 The mesoscale eddy moves westward at the speed of  $8 \text{ cm s}^{-1}$ . The speed of the cyclonically  
 619 rotating wind speed at the inertial frequency is set to  $13 \text{ m s}^{-1}$ .

620

621 The  $\alpha$  value also varies with the mesoscale eddy strength (Fig. 9b). The  $\alpha$  value decreases  
 622 significantly from about 6.66 to 1.60 for the  $|SLA_c|$  values in the range of 0.13 and 1.02 m. As  
 623 mentioned above, cyclonic eddies have limited ability in transferring their kinetic energy to NICs,  
 624 which differs significantly from anticyclonic eddies. However, stronger cyclonic eddies with more  
 625 eddy energy provide the more favorable condition for the energy transfer, which can narrow the  
 626 difference in the near-inertial energy transfer induced by anticyclonic eddies and cyclonic eddies.  
 627 Furthermore, stronger geostrophic currents lead to stronger geostrophic strain field which can  
 628 generate stronger NICs.

629 **5.6 Relative Vorticity and Strain**

630 As mentioned above, the anticyclonic eddies in the SML are more efficient than cyclonic  
 631 eddies for transferring kinetic energy to NICs, which can be explained by the relative vorticity of  
 632 the background flow ( $\zeta$ ) defined in Eq. (1). In numerical experiments, the direction of the energy  
 633 transfer is bidirectional, but primarily positive, that is, from mesoscale eddies to NICs. For  
 634 cyclonic eddies, the direction of the energy transfer is from the NICs to the cyclonic eddy under  
 635 cyclonically rotating winds at frequencies of  $0.25f$ ,  $0.75f$  and  $1.25f$  and anticyclonically rotating  
 636 winds at ~~frequencies frequency range~~ of  $-1.15f$  to  $-0.9f$  and  $-0.75f$ . When the frequencies of  
 637 anticyclonically rotating winds are range from  $-1.5f$  to  $-0.9f$ , the energy transfer is also negative  
 638 in the anticyclonic eddy. The  $\alpha$  value is more than 1.0 for about 8~~78~~8% of these experiments, which  
 639 indicates that the transferred near-inertial energy is larger in anticyclonic eddies than cyclonic  
 640 eddies.

641 In addition to the relative vorticity and translational speed of a mesoscale eddy, the normal  
 642 strain and shear strain of the background flow can also affect the energy transfer between the  
 643 mesoscale eddy and NICs in the SML. Jing et al. (2017) proposed a method to calculate the rate  
 644 of energy transfer from background mesoscale eddies to wind-induced NICs. Following Jing et al.  
 645 (2017), the energy transfer rate ( $\varepsilon$ ) between the NICs and the mesoscale eddy in the SML is given  
 646 as

$$647 \quad \varepsilon = -\rho H_{mix} (uuU_x + uvU_y + uvU_x + vvV_y), \quad (265)$$

648 where  $u$  and  $v$  are respectively the zonal and meridional components of the near-inertial current  
 649 velocity reproduced by the modified slab model, and subscripts  $x$  and  $y$  in  $U$  and  $V$  represent partial  
 650 derivatives. The positive  $\varepsilon$  mean the energy transfer from the mesoscale eddy to the NICs, and the  
 651 negative  $\varepsilon$  indicates the backward energy cascade. In the numerical experiments, the NICs can be  
 652 generated directly by the cyclonic winds, and the wind-induced NICs can further interact with the  
 653 mesoscale eddy and transfer the near-inertial energy from the mesoscale eddy to the NICs when  
 654 the mesoscale eddy passed by the nine locations P1-P9. Therefore, we also calculate the energy  
 655 transfer rate and Okubo-Weiss parameter at the nine fixed locations P1-P9 in the sensitivity  
 656 experiments ExpA3, ExpC1-C9 and ExpD1-D16, which are under the same wind conditions.

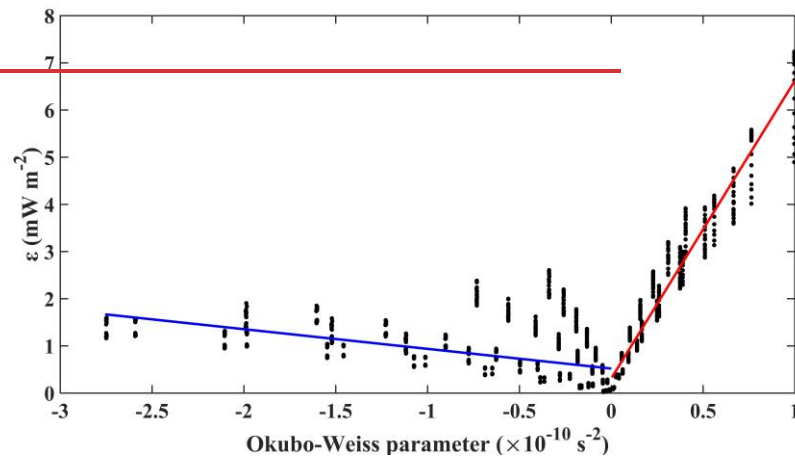
657 When the Okubo-Weiss parameters ([strains](#)) are negative, the energy transfer rate decreases  
 658 as the Okubo-Weiss parameter ([strain](#)) increases ([Fig. 10](#)). However, when the Okubo-Weiss

659 parameters (strains) are positive, the energy transfer rate shows an elevated trend with the increase  
660 of the Okubo-Weiss parameter (strain) (Fig. 10). Based on limited sensitivity studies, we found  
661 the relative vorticity and the strain of the mesoscale eddy both have an influence on the near-  
662 inertial energy transferred by interactions between mesoscale eddies and NICs.

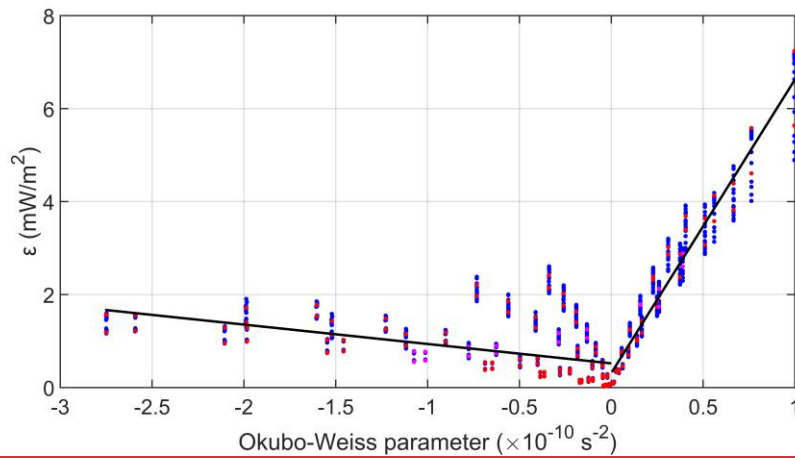
663

带格式的: 缩进: 首行缩进: 2 字符

664



665



666 **Figure 10.** Scatterplot between the energy transfer rate and the Okubo-Weiss parameter. Purple,  
667 blue and red dots respectively represent ExpA3, ExpC1-9 and ExpD1-16. The left (right) blue (red)  
668 line black line is the linear fitting line when the Okubo-Weiss parameters are negative  
669 (positive).

670 **6 Theoretical Analyses**671 **6.1 Solutions in the Frequency Domain**

672 To gain better understanding of the role of the relative vorticity in the background flow for  
 673 anticyclonic eddies to be significantly more efficient than the cyclonic eddies in transferring their  
 674 kinetic energy to NICs, we examine analytically the effect of the relative vorticity in the frequency  
 675 domain solution of the modified slab model.

676 The modified slab model can be written in the tensor form:

$$677 \frac{\partial}{\partial t} \begin{Bmatrix} u \\ v \end{Bmatrix} + \begin{bmatrix} a_1 & b_1 \\ a_2 & b_2 \end{bmatrix} \begin{Bmatrix} u \\ v \end{Bmatrix} = \begin{Bmatrix} c_1 \\ c_2 \end{Bmatrix}, \quad (276)$$

678 where,  $a_1 = U_x + r$ ,  $a_2 = V_x + f$ ,  $b_1 = U_y - f$ ,  $b_2 = V_y + r$ ,  $c_1 = \tau_x / \rho H_{mix}$  and  $c_2 = \tau_y / \rho H_{mix}$ . For simplicity, we consider the steady wind forcing to eliminate the wind induced NICs here. Under the steady winds, the NICs produced by the original slab model are zero, therefore the NICs produced by the modified slab model directly represent the near-inertial energy converted between mesoscale eddies and NICs. For simplicity, we consider the steady wind forcing to directly eliminate the wind-induced NICs here. In the case of steady winds, we use the Fourier transform to translate the modified slab model from the time domain into the frequency domain:

$$685 \begin{bmatrix} a_1 + i\omega & b_1 \\ a_2 & b_2 + i\omega \end{bmatrix} \begin{Bmatrix} \tilde{u} \\ \tilde{v} \end{Bmatrix} = \begin{Bmatrix} \tilde{c}_1 \\ \tilde{c}_2 \end{Bmatrix}, \quad (287)$$

686 where  $\omega$  is the frequency and variables with a tilde represent the values after Fourier transform.

687 Assuming the mesoscale eddy is in an almost steady state during an inertial period (Jing et al.  
 688 2017), the analytical solution for the zonal and meridional components of NICs in the frequency  
 689 domain can be written as

$$690 \tilde{u} = \frac{(b_2 + i\omega) \cdot 2\pi c_1 \delta(\omega) - b_1 \cdot 2\pi c_2 \delta(\omega)}{(a_1 + i\omega)(b_2 + i\omega) - a_2 b_1}, \quad (298)$$

$$691 \tilde{v} = \frac{(a_1 + i\omega) \cdot 2\pi c_2 \delta(\omega) - a_2 \cdot 2\pi c_1 \delta(\omega)}{(a_1 + i\omega)(b_2 + i\omega) - a_2 b_1}, \quad (3029)$$

692 where  $\delta(\omega)$  is the Dirac Delta function.

693 Based on Perceval's theorem, the energy of NICs is the same in both the time and frequency  
 694 domains:

$$695 \frac{1}{T} \int |U(t)|^2 dt = \int |U(\omega)|^2 d\omega, \quad (310)$$

696 where  $T$  is the total period.

697 The time-mean near-inertial kinetic energy  $\overline{U_{NIW_s}^2}$  in the time domain can be written as

$$698 \quad \overline{U_{NIW_s}^2} = \overline{u^2} + \overline{v^2}, \quad (324)$$

$$699 \quad \overline{u^2} = \int \frac{(b_2 c_1 - b_1 c_2)^2 + \omega^2 c_1^2 \cdot ((2\pi\delta(\omega))^2)}{(a_2 b_1 - a_1 b_2 + \omega^2)^2 + \omega^2 (a_1 + b_2)^2} \cdot d\omega, \quad (322)$$

$$700 \quad \overline{v^2} = \int \frac{(a_1 c_2 - a_2 c_1)^2 + \omega^2 c_2^2 \cdot ((2\pi\delta(\omega))^2)}{(a_2 b_1 - a_1 b_2 + \omega^2)^2 + \omega^2 (a_1 + b_2)^2} \cdot d\omega. \quad (343)$$

701 For a unidirectional laterally sheared geostrophic flow and the southwestward wind,  $U=0$ ,  
 702  $V=V(x)$ ,  $c_1 < 0$  and  $c_2 < 0$ . Substitution of  $a_1 = r$ ,  $a_2 = \zeta + f$ ,  $b_1 = -f$  and  $b_2 = r$  into Eq.  
 703 (3233) and Eq. (3334) yields

$$704 \quad \overline{u^2} = \int \frac{(rc_1 + fc_2)^2 + \omega^2 c_1^2 \cdot ((2\pi\delta(\omega))^2)}{(r^2 - \omega^2 + f(\zeta + f))^2 + 4\omega^2 r^2} d\omega, \quad (354)$$

$$705 \quad \overline{v^2} = \int \frac{(rc_2 - (\zeta + f)c_1)^2 + \omega^2 c_2^2 \cdot ((2\pi\delta(\omega))^2)}{(r^2 - \omega^2 + f(\zeta + f))^2 + 4\omega^2 r^2} d\omega. \quad (355)$$

706 Since the relative vorticity is negative in anticyclonic eddies, the denominator term for  $\overline{u^2}$  in  
 707 Eq. (3435) is less than the value with positive the relative vorticity to be positive. Therefore, the  
 708 value of  $\overline{u^2}$  is greater in anticyclonic eddies than in cyclonic eddies. For the positive relative  
 709 vorticity, the numerator term of  $\overline{v^2}$  is smaller and the denominator term in Eq. (3536) becomes  
 710 larger than the case of negative vorticity. This indicates that  $\overline{v^2}$  is more elevated in the anticyclonic  
 711 eddies. Since both  $\overline{u^2}$  and  $\overline{v^2}$  are elevated when the relative vorticity is negative than counterparts  
 712 with the positive relative vorticity, anticyclonic eddies can transfer more near-inertial energy than  
 713 cyclonic eddies.

## 714 6.2 Analytical Solution

715 An analytical solution based on the modified slab model is considered here to demonstrate  
 716 that mesoscale eddies can transfer more near-inertial energy for stronger winds. The modified  
 717 slab model can be written as

$$718 \quad \frac{\partial u}{\partial t} + a_1 u + b_1 v = c_1, \quad (376)$$

$$719 \quad \frac{\partial v}{\partial t} + a_2 u + b_2 v = c_2, \quad (387)$$

720 where,  $a_1 = U_x + r$ ,  $a_2 = V_x + f$ ,  $b_1 = U_y - f$ ,  $b_2 = V_y + r$ ,  $c_1 = \tau_x / \rho H_{mix}$ ,  $c_2 = \tau_y / \rho H_{mix}$ ,  
 721  $\tau_x = A \cos ft$  and  $\tau_y = A \sin ft$ .

722 For the cyclonic wind, substitution of Eq. (3637) into Eq. (3738) yields

$$723 \quad \frac{\partial^2 u}{\partial t^2} + (a_1 + b_2) \frac{\partial u}{\partial t} + (a_1 b_2 - a_2 b_1) u = b_2 c_1 - (f + b_1) c_2 \quad (398)$$

$$724 \quad \Delta = (a_1 + b_2)^2 - 4(a_1 b_2 - a_2 b_1). \quad (4039)$$

725 The analytical solutions of the current to the modified slab model are

$$726 \quad u_{Modified} = e^{\gamma t} (Q_1 \cos \beta t + Q_2 \sin \beta t) + Q_3 \cos ft + Q_4 \sin ft, \quad (410)$$

$$727 \quad v_{Modified} = \frac{1}{b_1} (c_1 - e^{\gamma t} (a_1 + \gamma) (Q_1 \cos \beta t + Q_2 \sin \beta t))$$

$$728 \quad -e^{\gamma t} \beta (Q_2 \cos \beta t - Q_1 \sin \beta t) + (f Q_3 - a_1 Q_4) \sin ft - (f Q_4 + a_1 Q_3) \cos ft, \quad (424)$$

729 where

$$730 \quad \gamma = -\frac{a_1 + b_2}{2}, \quad (432)$$

$$731 \quad \beta = \frac{\sqrt{-\Delta}}{2}, \quad (443)$$

$$732 \quad Q_1 = -Q_3, \quad (454)$$

$$733 \quad Q_2 = \frac{c_1 + \gamma Q_3 - f Q_4}{\beta}, \quad (465)$$

$$734 \quad Q_3 = \frac{A b_2 (a_1 b_2 - a_2 b_1 - f^2) + A (f + b_1) (f a_1 + f b_2)}{\rho H_{mix} ((a_1 b_2 - a_2 b_1 - f^2)^2 + (f a_1 + f b_2)^2)}, \quad (476)$$

$$735 \quad Q_4 = \frac{\rho H_{mix} Q_3 (f a_1 + f b_2) - A (f + b_1)}{\rho H_{mix} (a_1 b_2 - a_2 b_1 - f^2)}. \quad (487)$$

736 Increasing the wind stress  $c_1$  and  $c_2$  by a factor of  $n$  named  $c'_1$  and  $c'_2$  yields

$$737 \quad c'_1 = n c_1 = \frac{n \tau_x}{\rho H_{mix}} = \frac{n A \cos ft}{\rho H_{mix}}, \quad (498)$$

$$738 \quad c'_2 = n c_2 = \frac{n \tau_y}{\rho H_{mix}} = \frac{n A \sin ft}{\rho H_{mix}}. \quad (5049)$$

739 Substitution of  $c'_1$  and  $c'_2$  into  $Q_3$  and  $Q_4$  yields

$$740 \quad Q'_3 = \frac{n A b_2 (a_1 b_2 - a_2 b_1 - f^2) + n A (f + b_1) (f a_1 + f b_2)}{\rho H_{mix} ((a_1 b_2 - a_2 b_1 - f^2)^2 + (f a_1 + f b_2)^2)} = n Q_3, \quad (510)$$

$$741 \quad Q'_4 = \frac{\rho H_{mix} n Q_3 (f a_1 + f b_2) - n A (f + b_1)}{\rho H_{mix} (a_1 b_2 - a_2 b_1 - f^2)} = n Q_4. \quad (524)$$

742 Substitution of  $Q_3$  and  $Q_4$  into  $Q_1$  and  $Q_2$  yields

$$743 \quad Q'_1 = -n Q_3 = n Q_1, \quad (532)$$

$$744 \quad Q'_2 = \frac{n c_1 + \gamma n Q_3 - f n Q_4}{\beta} = n Q_2. \quad (543)$$

745 Therefore, the current with the increased wind stress to the modified slab model is given as

$$746 \quad u_{Modified}' = n u_{Modified}, \quad (554)$$

$$747 \quad v_{Modified}' = n v_{Modified}. \quad (565)$$

748 The analytical solution of the current to the original slab model is

749 
$$U_{Original} = \frac{Ae^{ift}}{\rho H_{mix}(if+r)} + \left( \left( \frac{Ae^{-(if+r)t}}{\rho H_{mix}(if+r)} \right) \left( \frac{if}{2if+r} \right) (1 - e^{(2if+r)t}) \right) - \frac{Ae^{-(if+r)t}}{\rho H_{mix}(if+r)}. \quad (576)$$

750 Therefore, the current with the increased wind stress to the original slab model is given as

751 
$$U_{Original}' = nU_{Original}. \quad (587)$$

752 The above analytical solutions demonstrate that when the wind stress increases by  $n$  times,  
753 the current speeds simulated by the modified and original slab models both increase by  $n$  times.  
754 The differences in the average speeds of NICs between the modified and original model represent  
755 the transferred near-inertial energy by the interaction between mesoscale eddies and near-inertial  
756 motions (Eq. (2122) and (2223)). As the NICs are the component of the total currents in the near-  
757 inertial frequency band, the transferred near-inertial energy in the mesoscale eddies also increases  
758 by a factor of  $n$  times when the wind stress is multiplied by  $n$  times. This feature is consistent with  
759 our sensitivity experiments in Sect. 5.

## 760 7 Summary and Discussion

761 Analysis of in situ current observations at two offshore ADCP mooring sites in the northern  
762 South China Sea (nSCS) demonstrated that relatively strong near-inertial currents (NICs) occurred  
763 during certain periods of nearly steady winds in the lower part of the ocean surface mixed layer  
764 (SML). The NICs produced by the original slab model are significantly larger than the observations,  
765 indicating other important processes operating over the area. We followed Welle (1982) and Jing  
766 et al. (2017) and used a modified slab model in this study by including contributions from the  
767 background geostrophic currents. Using the surface geostrophic currents inferred from the satellite  
768 sea level data and assuming the geostrophic currents in the SML is vertically uniform, we found  
769 that the modified slab model performs significantly better than the original slab model in  
770 reproducing the observed NICs at two ADCP mooring sites in the nSCS. Examinations of  
771 observations and numerical results produced by the modified and original slab models revealed  
772 the occurrence of the energy exchange between the mesoscale eddies and the NICs. Based on the  
773 energy budget analysis for NICs during the observational period, the difference of the near-inertial  
774 wind power input between the original slab model and the modified slab model is the same order  
775 as the energy transfer rate (Eq. 2526). This also indicates the importance of the near-inertial energy

776 transfer induced by the interaction between mesoscale eddies and NICs in the SML during the  
777 observational period.

778 The modified slab model and original slab model were then used to examine sensitivity to  
779 winds and eddy parameters with idealized mesoscale eddies under cyclonic winds. Both cyclonic  
780 and anticyclonic mesoscale eddies were considered, using the universal eddy structure suggested  
781 by Zhang et al. (2013). One of our major findings is that anticyclone eddies can transfer more  
782 kinetic energy to NICs than cyclonic eddies. Idealized experiments show that induced NICs speed  
783 in anticyclonic eddies can reach over 6 times the speed in cyclonic eddies. We also found that the  
784 energy transfer rate is related to the Okubo-Weiss parameter. When the Okubo-Weiss parameter  
785 is positive, the energy transfer rate is elevated with the larger Okubo-Weiss parameter.

786 Analyses of model results in 196 numerical experiments using the modified slab model  
787 demonstrated that there exists bidirectional energy transfer between mesoscale eddies and NICs.  
788 The direction of the energy transfer is primarily from mesoscale eddies to NICs. When the cyclonic  
789 winds rotate at frequencies of  $0.25f$ ,  $0.75f$  and  $1.25f$  and the anticyclonic winds rotate at  
790 frequencies ~~of ranging from~~  $-1.15f$ , ~~0.9f and to~~  $-0.75f$ , the direction of the energy transfer is  
791 negative in the cyclonic eddy, that is, from NICs to cyclonic eddies. Under anticyclonically  
792 rotating winds at ~~the frequency rangeies~~ of  $-1.5f$  ~~to, -1.25f, -1.1f and -0.99f~~, the negative energy  
793 transfer also occurs in the anticyclonic eddy. The NICs transferred from mesoscale eddies are  
794 stronger for higher wind speeds, faster translational speeds and stronger strengths of mesoscale  
795 eddies. When the wind stress increases by a factor of  $n$  times, the amplitudes of the converted  
796 NICs are also multiplied by  $n$  times. The NICs transferred in mesoscale eddies by the interactions  
797 between mesoscale eddies and NICs are stronger for higher translational speeds of anticyclonic  
798 eddies. At the translational speeds of  $11 \text{ cm s}^{-1}$ , the ratios of the amplitudes of the converted NICs  
799 by anticyclonic eddies to that transferred by cyclonic eddies reach maximum values.

800 For analytical considerations, the modified slab model was transferred from the time domain  
801 to the frequency domain using the Fourier transform. Using Parseval's theorem, we derived the  
802 time-mean value of the induced NICs. The analytical expression was used to demonstrate that, for  
803 the negative relative vorticity, i.e., such as within an anticyclonic eddy, the transferred NICs are  
804 larger in an anticyclonic eddy than a cyclonic eddy. The analytical solution under the cyclonic  
805 winds also demonstrated that the NICs transferred by mesoscale eddies increase linearly with the

806 wind stress. These analytical results are consistent with the results produced by the modified and  
807 original slab models.

808 We also conducted the same set of numerical experiments using steady winds in both constant  
809 speeds and direction and model results in the steady winds are not presented here due to the page  
810 limit. Our main findings on the energy transfer between mesoscale eddies and NICs in these  
811 experiments with the steady winds are the same as the results using the rotating winds.

812 This study suggests that there is bidirectional energy transfer between mesoscale eddies and  
813 NICs in the SML, of which the mechanism and influence factors are further explored by idealized  
814 simulations. Our findings can further contribute to the understanding of the energy budget in the  
815 global ocean and the ocean response to the climate change. In order to examine major physical  
816 processes affecting the NICs generated by the mesoscale eddies and quantify their influence on  
817 turbulent mixing in the deeper ocean, further studies are needed using a three-dimensional ocean  
818 circulation model.

819 **Data availability**

820 All the data can be obtained by contacting the authors.

821 **Competing interests**

822 The authors declare that they have no conflict of interest.

823 **Acknowledgments**

824 This study is supported by funds from the Guangdong Basic and Applied Basic Research  
825 Foundation (2022B1515130006), the National Natural Science Foundation of China (91958203)  
826 and Shenzhen Science and Technology Innovation Committee (WDZC20200819105831001). We  
827 thank the editor and reviewers for their useful and constructive comments.

828 **References**

829 Alford, M. H.: Improved global maps and 54-year history of wind-work on ocean inertial motions,  
830 Geophys. Res. Lett., 30(8), <https://doi.org/10.1029/2002GL016614>, 2003.

831 Alford, M. H., MacKinnon, J. A., & Simmons, H. L.: Near-inertial internal gravity waves in the  
832 ocean, *Ann. Rev. Mar. Sci.*, 8, 95–123, <https://doi.org/10.1146/annurev-marine-010814-015746>, 2016.

833

834 Barkan, R., Srinivasan, K., & Yang, L.: Oceanic mesoscale eddy depletion catalyzed by internal  
835 waves, *Geophys. Res. Lett.*, 48(18), e2021GL094376,  
836 <https://doi.org/10.1002/essoar.10507068.1>, 2021.

837 Boyer, T.P., O.K. Baranova, C. Coleman, H.E. Garcia, A. Grodsky, R.A. Locarnini, A.V.  
838 Mishonov, C.R. Paver, J.R. Reagan, D. Seidov, I.V. Smolyar, K.W. Weathers, & M.M.  
839 Zweng.: NOAA Atlas NESDIS 87, World Ocean Database 2018 [Dataset],  
840 <https://www.ncei.noaa.gov/access/world-ocean-atlas-2018/>, 2019.

841 Bühler, O., & McIntyre, M. E.: Wave capture and wave–vortex duality, *J. Fluid Mech.*, 534, 67–  
842 95. <https://doi.org/10.1017/S0022112005004374>, 2005.

843 Chelton, D. B., Schlax, M. G., & Samelson, R. M.: Global observations of nonlinear mesoscale  
844 eddies, *Prog. Oceanogr.*, 91(2), 167–216, <https://doi.org/10.1016/j.pocean.2011.01.002>,  
845 2011.

846 Chen, S.: OSF, The Current Observation Data (S2 and S3) in the Mixed Layer [Dataset],  
847 <https://doi.org/osf.io/r9kyz>, 2023.

848 Chen, S., J. Polton, Hu, J., & Xing, J.: Local inertial oscillations in the surface ocean generated by  
849 time-varying winds, *Ocean Dyn.*, 65, 1633–1641, <https://doi.org/10.1007/s10236-015-0899-6>, 2015a.

850

851 Chen, S., Hu, J. & J. A. Polton.: Features of near-inertial motions observed on the northern South  
852 China Sea shelf during the passage of two typhoons, *Acta Oceanol. Sin.*, 34, 38–43,  
853 <https://doi.org/10.1007/s13131-015-0594-y>, 2015b.

854 Chen, S., J. A. Polton, Hu, J., & Xing, J.: Thermocline bulk shear analysis in the northern North  
855 Sea, *Ocean Dyn.*, 66, 499–508, <https://doi.org/10.1007/s10236-016-0933-3>, 2016.

856 Chen, S., Chen, D. & Xing, J.: A study on some basic features of inertial oscillations and near-  
857 inertial internal waves, *Ocean Sci.*, 13, 829–836, <https://doi.org/10.5194/os-2017-33>, 2017.

858 Chen, G., Xue, H., & Wang, D.: Observed near-inertial kinetic energy in the northwestern South  
859 China Sea, *J. Geophys. Res.-Oceans*, 118(10), 4965–4977, <https://doi.org/10.5194/os-2017-33>, 2013.

860

861 Copernicus Climate Change Service, Climate Data Store.: Sea level gridded data from satellite  
862 observations for the global ocean from 1993 to present [Dataset],  
863 <https://doi.org/10.24381/cds.4c328c78>, 2018.

864 D'Asaro E. A.: The energy flux from the wind to near-inertial motions in the surface mixed layer,  
865 *J. Phys. Oceanogr.*, 15(8), 1043–1059, [https://doi.org/10.1175/1520-0485\(1985\)015<1043:tefttw>2.0.co;2](https://doi.org/10.1175/1520-0485(1985)015<1043:tefttw>2.0.co;2), 1985.

866

867 D'Asaro, E. A., Eriksen C. C., & Levine M. D.: Upper-ocean inertial currents forced by a  
868 strong storm. Part I: data and comparisons with linear theory, *J. Phys. Oceanogr.*, 25(11),  
869 2909–2936, [https://doi.org/10.1175/1520-0485\(1995\)025<2909:uoicfb>2.0.co;2](https://doi.org/10.1175/1520-0485(1995)025<2909:uoicfb>2.0.co;2), 1995.

870 Eliopon, S., Lumpkin, R., & Prieto, G.: Modification of inertial oscillations by the mesoscale eddy  
871 field, *J. Geophys. Res.-Oceans*, 115(C9), <https://doi.org/10.1029/2009jc005679>, 2010.

871

872 Fer, I., Bosse, A., Ferron, B., & Bouruet-Aubertot, P.: The dissipation of kinetic energy in the  
873 Lofoten Basin Eddy, *J. Phys. Oceanogr.*, 48(6), 1299–1316, <https://doi.org/10.1175/JPO-D-17-0244.1>, 2018.

域代码已更改

874  
875 Ferrari, R., & Wunsch, C.: Ocean circulation kinetic energy: Reservoirs, sources, and sinks, *Annu.*  
876 *Rev. Fluid Mech.*, 41, 253–282, <https://doi.org/10.1146/annurev.fluid.40.111406.102139>,  
877 2009.

878 Ford, R., McIntyre, M. E., & Norton, W. A.: Balance and the slow quasimaniifold: some explicit  
879 results, *J. Atmos. Sci.*, 57(9), 1236–1254, [https://doi.org/10.1175/1520-0469\(2000\)057<1236:BATSQS>2.0.CO;2](https://doi.org/10.1175/1520-0469(2000)057<1236:BATSQS>2.0.CO;2), 2000.

880 Garrett, C.: What is the “near-inertial” band and why is it different from the rest of the internal  
881 wave spectrum?, *J. Phys. Oceanogr.*, 31, 962–971, [https://doi.org/10.1175/1520-0485\(2001\)031,0962:WITNIB.2.0.CO;2](https://doi.org/10.1175/1520-0485(2001)031,0962:WITNIB.2.0.CO;2), 2001.

882 Gill A.: On the Behavior of Internal Waves in the Wakes of Storms, *J. Phys. Oceanogr.*, 14(7),  
883 1129–1151, [https://doi.org/10.1175/1520-0485\(1984\)014<1129:otboiw>2.0.co;2](https://doi.org/10.1175/1520-0485(1984)014<1129:otboiw>2.0.co;2), 1984.

884 Greatbatch, R. J.: On the response of the ocean to a travelling storm: Parameters and scales, *J.*  
885 *Phys. Oceanogr.*, 14, 59–78, [https://doi.org/10.1175/1520-0485\(1984\)014,0059:OTROTO.2.0.CO;2](https://doi.org/10.1175/1520-0485(1984)014,0059:OTROTO.2.0.CO;2), 1984.

886 Hersbach, H., Bell, B., Berrisford, P., Biavati, G., Horányi, A., Muñoz Sabater, J., Nicolas, J.,  
887 Peubey, C., Radu, R., Rozum, I., Schepers, D., Simmons, A., Soci, C., Dee, D., & Thépaut,  
888 J.-N.: Copernicus Climate Change Service (C3S) Climate Data Store (CDS), ERA5 hourly  
889 data on single levels from 1940 to present [Dataset], <https://doi.org/10.24381/cds.adbb2d47>, 2023.

890 Jaimes, B., & Shay, L.K.: Near-Inertial Wave Wake of Hurricanes Katrina and Rita over Mesoscale  
891 Oceanic Eddies, *J. Phys. Oceanogr.*, 40(6), 1320–1337,  
892 <https://doi.org/10.1175/2010JPO4309.1>, 2010.

893 Jing, Z., Wu, L., & Ma, X.: Sensitivity of near-inertial internal waves to spatial interpolations of  
894 wind stress in ocean generation circulation models, *Ocean Modell.*, 99, 15–21,  
895 <https://doi.org/10.1016/j.ocemod.2015.12.006>, 2016.

896 Jing, Z., Wu, L., & Ma, X.: Energy exchange between the mesoscale oceanic eddies and wind-  
897 forced near-inertial oscillations, *J. Phys. Oceanogr.*, 47(3), 721–733,  
898 <https://doi.org/10.1175/JPO-D-16-0214.1>, 2017.

899 Jing, Z., Chang, P., DiMarco, S.F., & Wu, L.: Observed energy exchange between low-frequency  
900 flows and internal waves in the Gulf of Mexico, *J. Phys. Oceanogr.*, 48, 995–1008,  
901 <https://doi.org/10.1175/JPO-D-17-0263.1>, 2018.

902 Jochum, M., Briegleb, B., Danabasoglu, G., Large, W., Norton, N., Jayne, S., Alford, M., & Bryan,  
903 F.: The impact of oceanic near-inertial waves on climate, *J. Clim.*, 26, 2833–2844,  
904 <https://doi.org/10.1175/JCLI-D-12-00181.1>, 2013.

905 Kunze, E.: Near-inertial wave propagation in geostrophic shear, *J. Phys. Oceanogr.*, 15(5), 544–  
906 565, [https://doi.org/10.1175/1520-0485\(1985\)015<0544:NIWPIG>2.0.CO;2](https://doi.org/10.1175/1520-0485(1985)015<0544:NIWPIG>2.0.CO;2), 1985.

907 Lelong, M. P., Cuypers, Y., & Bouruet-Aubertot, P.: Near-inertial energy propagation inside a  
908 Mediterranean anticyclonic eddy, *J. Phys. Oceanogr.*, 50(8), 2271–2288,  
909 <https://doi.org/10.1175/JPO-D-19-0211.1>, 2020.

域代码已更改  
设置了格式: 字体: (中文) 等线, 无下划线, 字体颜色: 文字 1

域代码已更改

915  
916 Liu, G., Chen, Z., Lu, H., Liu, Z., Zhang, Q., He, Q., He, Y., Xu, J., Gong, Y., & Cai, S.: Energy  
917 transfer between mesoscale eddies and near-inertial waves from surface drifter  
918 observations, *Geophys. Res. Lett.*, 50, e2023GL104729,  
919 <https://doi.org/10.1029/2023GL104729>, 2023.

920 McWilliams, J. C.: Submesoscale currents in the ocean, *Proc. R. Soc. A.*, 472(2189), 20160117,  
921 <https://doi.org/10.1098/rspa.2016.0117>, 2016.

922 Mooers, C. N.: Several effects of a baroclinic current on the cross-stream propagation of inertial-  
923 internal waves, *Geophys. Fluid Dyn.*, 6(3), 245–275,  
924 <https://doi.org/10.1080/03091927509365797>, 1975.

925 Muller, P.: On the diffusion of momentum and mass by internal gravity waves, *J. Fluid Mech.*,  
926 77(4), 789–823, <https://doi.org/10.1017/S0022112076002899>, 1976.

927 Munk, W., & Wunsch, C.: Abyssal recipes II: Energetics of tidal and wind mixing, *Deep-Sea Res. Pt. I*, 45, 1977–2010, [https://doi.org/10.1016/S0967-0637\(98\)00070-3](https://doi.org/10.1016/S0967-0637(98)00070-3), 1998.

928 Noh, S., & Nam, S.: Observations of enhanced internal waves in an area of strong mesoscale  
929 variability in the southwestern East Sea (Japan Sea), *Sci. Rep.*, 10, 9068,  
930 <https://doi.org/10.1038/s41598-020-65751-1>, 2020.

931 Oey, L. Y., Ezer, T., & Wang, D. P.: Loop current warming by hurricane Wilma, *Geophys. Res. Lett.*, 33(8), L08613, <https://doi.org/10.1029/2006GL025873>, 2006.

932 Okubo, A.: Horizontal dispersion of floatable particles in the vicinity of velocity singularities such  
933 as convergences, *Deep. Sea Res. Oceanogr. Abstr.*, 17(3), 445–454,  
934 [https://doi.org/10.1016/0011-7471\(70\)90059-8](https://doi.org/10.1016/0011-7471(70)90059-8), 1970.

935 Paduan, J. D., Szoelke, R. A., & Weller, R. A.: Inertial oscillations in the upper ocean during the  
936 Mixed Layer Dynamics Experiment (MILDEX), *J. Geophys. Res.*, 94, 4835–4842,  
937 <https://doi.org/10.1029/JC094iC04p04835>, 1989.

938 Perkins, H.: Observed effect of an eddy on inertial oscillations, *Deep. Sea Res. Oceanogr. Abstr.*,  
939 23(11), 1037–1042, [https://doi.org/10.1016/0011-7471\(76\)90879-2](https://doi.org/10.1016/0011-7471(76)90879-2), 1976.

940 Pollard, R. T., & Millard, R. C.: Comparison between observed and simulated wind-generated  
941 inertial oscillations, *Deep. Sea Res. Oceanogr. Abstr.*, 17, 813–816,  
942 [https://doi.org/10.1016/0011-7471\(70\)90043-4](https://doi.org/10.1016/0011-7471(70)90043-4), 1970.

943 Price, J. F., Weller, R. A., & Pinkel, R.: Diurnal cycling: Observations and models of the upper  
944 ocean response to diurnal heating, cooling, and wind mixing, *J. Geophys. Res.*, 91, 8411–  
945 8427, <https://doi.org/10.1029/JC091iC07p08411>, 1986.

946 Shu, Y., Wang, Q., & Zu, T.: Progress on shelf and slope circulation in the northern South China  
947 Sea, *Sci. China Earth Sci.*, 61, 560–571, <https://doi.org/10.1007/s11430-017-9152-y>, 2018.

948 Sun, Z., Hu, J., & Zheng, Q.: Strong near-inertial oscillations in geostrophic shear in the northern  
949 South China Sea, *J. Oceanogr.*, 67(4), 377–384, <https://doi.org/10.1007/s10872-011-0038-z>, 2011.

950 Thomas, L. N.: On the effects of frontogenetic strain on symmetric instability and inertia-gravity  
951 waves, *J. Fluid Mech.*, 711, 620–640, <https://doi.org/10.1017/jfm.2012.416>, 2012.

952 Thomas, L. N.: On the modifications of near-inertial waves at fronts: Implications for energy  
953 transfer across scales, *Ocean Dyn.*, 67(10), 1–16, <https://doi.org/10.1007/s10236-017-1088-6>, 2017.

域代码已更改

958 van Meurs, P.: Interactions between near-inertial mixed layer currents and the mesoscale: the  
959 importance of spatial variabilities in the vorticity field, *J. Phys. Oceanogr.*, 28(7), 1363–  
960 1388, [https://doi.org/10.1175/1520-0485\(1998\)0282.0.CO;2](https://doi.org/10.1175/1520-0485(1998)0282.0.CO;2), 1998.

961 Vanneste, J.: Balance and spontaneous wave generation in geophysical flows, *Annu. Rev. Fluid  
962 Mech.*, 45, 147–172, <https://doi.org/10.1146/annurev-fluid-011212-140730>, 2013.

963 Wang, Y., Guan, S., Zhang, Z., Zhou, C., Xu, X., Guo, C., Zhao, W. & Tian, J.: Observations of  
964 Parametric Subharmonic Instability of Diurnal Internal Tides in the Northwest Pacific, *J.  
965 Phys. Oceanogr.*, 54(3), 849–870, <https://doi.org/10.1175/JPO-D-23-0055.1>, 2024.

966 Weller, R. A.: The relation of near-inertial motions observed in the mixed layer during the JASIN  
967 (1978) experiment to the local wind stress and to the quasi-geostrophic flow field, *J. Phys.  
968 Oceanogr.*, 12, 1122–1136, [https://doi.org/10.1175/1520-0485\(1982\)0122.0.CO;2](https://doi.org/10.1175/1520-0485(1982)0122.0.CO;2), 1982.

969 Wei, Z., Xue, H., & Qin, H.: Using idealized numerical experiment to study an eddy colliding with  
970 an island, *J. Trop. Oceanogr.*, 36(4), 35–47, <https://doi.org/10.11978/2016118>, 2017.

971 Whalen, C. B., Lavergne, C. D., Garabato, A. C. N., Klymak, J. M., & Sheen, K. L.: Internal wave-  
972 driven mixing: Governing processes and consequences for climate, *Nat Rev Earth Environ.*,  
973 1(11), 606–621, <https://doi.org/10.1038/s43017-020-0097-z>, 2020.

974 Whitt, D. B., & L. N. Thomas.: Resonant generation and energetics of wind-forced near-inertial  
975 motions in a geostrophic flow, *J. Phys. Oceanogr.*, 45, 181–208,  
976 <https://doi.org/10.1175/JPO-D-14-0168.1>, 2015.

977 Wunsch, C., & Ferrari, R.: Vertical mixing, energy and the general circulation of the oceans, *Annu.  
978 Rev. Fluid Mech.*, 36, 281–314, <https://doi.org/10.1146/annurev.fluid.36.050802.122121>,  
979 2004.

980 Xie, J., & Vanneste, J.: A generalised-Lagrangian-mean model of the interactions between near-  
981 inertial waves and mean flow, *J. Fluid Mech.*, 774, 143–169,  
982 <https://doi.org/10.1017/jfm.2015.251>, 2015.

983 Young, W. R., & Jelloul, M. B.: Propagation of near-inertial oscillations through a geostrophic  
984 flow, *J. Mar. Res.*, 55(4), 735–766, <https://doi.org/10.1357/0022240973224283>, 1997.

985 Zhai, X., Greatbatch, R. & Zhao, J.: Enhanced vertical propagation of storm-induced near-inertial  
986 energy in an eddying ocean channel, *Geophys. Res. Lett.*, 32(18), L18602,  
987 <https://doi.org/10.1029/2005GL023643>, 2005.

988 Zhai, X., Greatbatch, R. J. & Eden, C.: Spreading of near-inertial energy in a 1/12° model of the  
989 North Atlantic Ocean, *Geophys. Res. Lett.*, 34(10), 421–428,  
990 <https://doi.org/10.1029/2007GL029895>, 2007.

991 Zhang, Z., Zhang, Y., & Wang, W.: Universal structure of mesoscale eddies in the ocean, *Geophys.  
992 Res. Lett.*, 40(14), 3677–3681, <https://doi.org/10.1002/grl.50736>, 2013.